Analysis of a Destructive Wind Storm on 16 November 2008 in Brisbane, Australia

HARALD RICHTER AND JUSTIN PETER

Centre for Australian Weather and Climate Research, Bureau of Meteorology, Melbourne, Victoria, Australia

SCOTT COLLIS

Environmental Science Division, Argonne National Laboratory, Downers Grove Township, Illinois

(Manuscript received 18 December 2013, in final form 15 May 2014)

ABSTRACT

During the late afternoon on 16 November 2008 the Brisbane (Queensland, Australia) suburb of "The Gap" experienced extensive wind damage caused by an intense local thunderstorm. The CP2 research radar nearby detected near-surface radial velocities exceeding 43 m s^{-1} above The Gap while hail size reports did not exceed golf ball size, and no tornadoes were reported. The storm environment was characterized by a layer of very moist near-surface air and strong storm-relative low-level flow, whereas the storm-relative winds aloft were weak. While the thermodynamic storm environment contained a range of downdraft-promoting ingredients such as a ~4-km-high melting level above a ~2-km-deep layer with nearly dry-adiabatic lapse rates mostly collocated with dry ambient air, a ~1-km-deep stable layer near the ground would generally lower expectations of destructive surface winds based on the downburst mechanism. Once observed reflectivities exceed 70 dB*Z*, downdraft cooling due to hail melting and downdraft acceleration based on hail loading are found to likely become nonnegligible forcing mechanisms. The event featured the close proximity of a hydrostatically and dynamically driven mesohigh at the base of the downdraft to a dynamically driven mesolow associated with a low-level circulation. This proximity was instrumental in the anisotropic horizontal acceleration of the near-ground outflow and the ultimate strength of the Gap storm surface winds. Weak storm-relative midlevel winds are speculated to have allowed the downdraft to descend close to the low-level circulation, which set up this strong horizontal perturbation pressure gradient.

1. Introduction

Damaging straight-line winds are perhaps the most common convectively generated hazard associated with severe thunderstorms (Kelly et al. 1985; Hurlbut and Cohen 2014). Particular attention is warranted for storm modes that are most likely to produce particularly strong straight-line surface winds—derechos (Johns and Hirt 1987) and high-precipitation (HP) supercells (Moller et al. 1990). At least observationally this includes the pursuit of a better understanding of storm environmental attributes that are characteristic of high-end wind storms.

Coniglio et al. (2011) found that the primary difference between the 8 May 2009 derecho environment and a more general mesoscale convective system (MCS; Houze 2004) environment was a strong and deep low-level jet (Tuttle and Davis 2006) that was transporting anomalously high mixing ratio air toward the storm underneath anomalously large midtropospheric lapse rates. Interestingly, these ingredients are primarily promoting stronger updrafts, rather than stronger downdrafts. Evans and Doswell (2001) previously considered 67 derecho environments and also pointed to strong 0–2-km above ground level (AGL) system-relative flow and reasonably steep 700–500-hPa lapse rates, the former again being a feature that distinguished derecho environments from nonsevere MCS environments in their study. Curiously, though, the 67 derechos occurred over a very wide range of shear and instability measures.

One additional environmental characteristic of the derecho environments documented in Evans and Doswell (2001) is the relatively weak system-relative midtropospheric winds. The middle 50% of the 4–6-km system-relative winds in their derecho distribution were between 5.5 and 10.5 m s^{-1}. Such weak system-relative flows have

Corresponding author address: Harald Richter, Centre for Australian Weather and Climate Research, Bureau of Meteorology, GPO Box 1289K, Melbourne, VIC 3001, Australia.
E-mail: h.richter@bom.gov.au

DOI: 10.1175/MWR-D-13-00405.1

also been highlighted as a noteworthy feature in a series of conference papers on extreme wind-producing storms such as the Lahoma, Oklahoma, storm on 17 August 1994 (Conway et al. 1996; Lemon and Parker 1996), which resembled similar largely nontornadic prior events such as the Pakwash (Ontario, Canada) 18 July 1991 storm and others (Brooks and Doswell 1993). Eyre (1992) added two Australian events to this collection. In most of these extreme wind cases, however, the underlying storm was an HP supercell rather than an MCS or a derecho, the latter being a convective windstorm produced by a small subset of MCSs (Johns and Hirt 1987). Moller et al. (1994) found that it is particularly the high-precipitation end of the supercell spectrum that tends to produce strong straight-line winds and large hail, a finding that reaffirms the already known strong connection between heavy precipitation and damaging surface winds.

Most downdrafts are driven thermodynamically through the evaporation of liquid water, melting of ice, and sublimation of ice. Each of these phase changes cools the surrounding air and increases its density, which is equivalent to the generation of negative buoyancy. Hydrometeor loading is an additional downward directed force that is believed to be of secondary importance in forcing downdrafts [see p. 260 in (Wakimoto 2001)]. A range of idealized modeling studies found that the effectiveness of phase changes to generate a negatively buoyant downdraft is strongly dependent on the storm environment. Kamburova and Ludlam (1966), Srivastava (1985, hereafter S85; 1987), and Proctor (1989, hereafter P89) all agree that strong convectively driven downdrafts are promoted by a core of very large hydrometeor mixing ratios descending through a dry-adiabatic subcloud layer. S85 and P89 also point out that narrow downdrafts (downdraft diameters of ~2 km or less) are increasingly vulnerable to the entrainment of ambient air and the dilution of their negative buoyancy, and that a very humid layer of air near the ground promotes additional downdraft acceleration due to a higher virtual temperature (lower density) of the environmental air. P89, extending the rain-only simulations of S85 by including ice, also emphasizes that intense microbursts benefit from high melting levels overlaying a layer of dry air with steep lapse rates. These environmental ingredients allow large amounts of hail to melt, and for the resulting liquid water to evaporate in an environment that is rapidly warming as the downdraft descends.

P89 and Wakimoto (2001) stress that the downdraft strength (characterized by a representative downward velocity W) is not necessarily a reliable indicator of the magnitude of the horizontal surface wind U in the thunderstorm outflow. P89 refers to the $U = U(W)$ relationship as *seemingly erratic* given it is influenced by a range of parameters including the hydrometeor types and size distributions, the outflow depth and density gradient across the cold pool boundary (Benjamin 1968), among other factors.

Wakimoto (2001) also reviewed an additional dynamical forcing mechanism for downdrafts that is specific to supercells. While the rear-flank downdraft (RFD) of a supercell certainly has thermodynamic and hydrometeor loading forcing components, downward-pointing dynamically induced vertical pressure gradients may play an additional role. Based on numerical simulations, Klemp and Rotunno (1983) define the *occlusion downdraft* to be the section of the RFD that is induced by a downward-directed vertical perturbation pressure gradient associated with strong low-level rotation on the storm scale. Wakimoto et al. (1996) later confirmed the existence of such an occlusion downdraft using airborne Doppler radar observations. It stands to reason that the storm-scale perturbation low pressure associated with low-level rotation cannot only accelerate air parcels downward, but also horizontally in order to create damaging winds at the surface. This way, a downdraft parcel descending at some horizontal distance from the axis of low-level rotation (Markowski 2002) can be accelerated not only downward but also horizontally from the cold pool mesohigh toward the circulation-induced low.

This study examines how a multicell–HP supercell hybrid storm that formed in a seemingly marginal severe thunderstorm environment on 16 November 2008 was able to cause extensive wind damage over an area exceeding 20 km^2 in the densely populated suburb of "The Gap," located about 10 km west-northwest of the center of Brisbane, Queensland, Australia. Peak radial winds reached about 43 m s^{-1} near the surface, with hail up to golf-ball size reported. Fortunately, as part of the Queensland Cloud Seeding Research Program (Tessendorf et al. 2012), the storm was not only observed by the operational S-band Doppler radar, Mount Stapylton, but also a second, polarimetric S-band Doppler radar, CP2.

2. Evolution of the larger-scale prestorm environment

On the synoptic scale, water vapor loops supported by numerical model analyses (not shown) show a progressive eastward-moving vertically stacked low over the southern Tasman Sea (Fig. 1). Upper-level ridging was apparent over the northern parts of Queensland (QLD) and the adjacent oceans. A broad, cyclonically curved diffluent 300-hPa jet extended into southern QLD from the south.

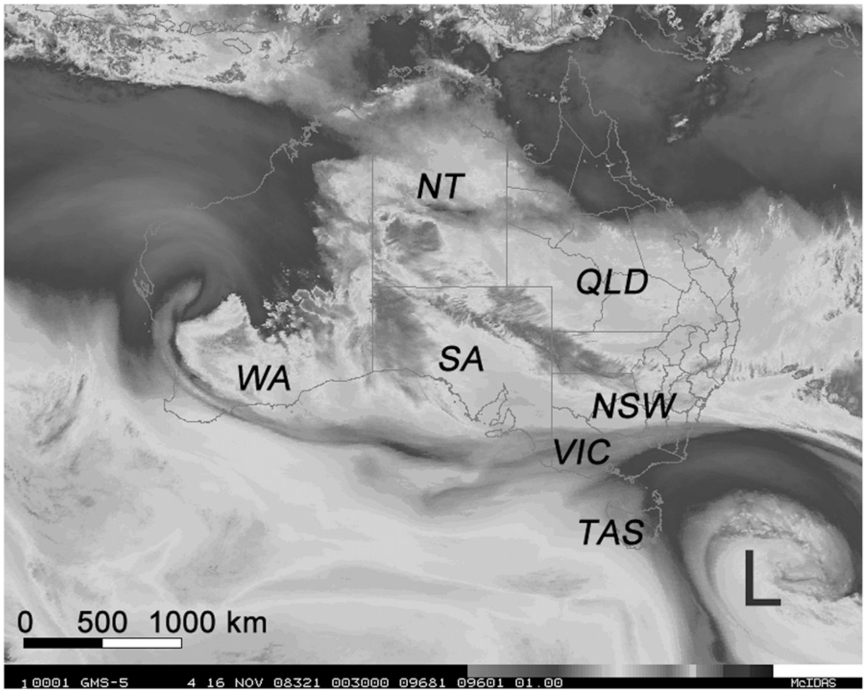

FIG. 1. Water vapor image at 0030 UTC 16 Nov 2008. Overlaid are the names of the Australian states and territories (Australian Capital Territory excepted): Western Australia, WA; Northern Territory, NT; South Australia, SA; Queensland, QLD; New South Wales, NSW; Victoria, VIC; and Tasmania, TAS. The low pressure system in the southern Tasman Sea referred to in the text is marked by a capital el (L).

A surface front extended from a 992-hPa surface low in the southern Tasman Sea through the northeastern corner of New South Wales (NSW) into central and western QLD during the morning (0100 UTC 16 November 2008; LT = UTC + 10 h; Fig. 2). Along its northern segments, this boundary generally separated warmer and moister air with north-to-northeasterly flow to the northeast from drier and cooler air to the southwest (Fig. 2). Near the coast south of Brisbane the front was a relatively sharp east–west running boundary at 0100 UTC (1100 LT) along which the first storms initiated around 0030 UTC. By 0430 UTC storms initiated almost all the way to the western border of QLD (Fig. 3). The probability of encountering severe thunderstorms increased from west to east along the boundary, as can be broadly inferred from the temporally consistent size and spread of the storm anvils in Fig. 3, radar imagery (not shown), or the few available severe weather reports.

Deep-layer shear values were maximized in the southeastern corner of QLD in the vicinity of the mid- and upper-level jets, especially in locations where northeasterly surface winds resided underneath the enhanced westerly midlevel flow. The observed 500-hPa winds at 2300 UTC 15 November reached 17.5 m s^{-1} in Moree and 12.5 m s^{-1} at Brisbane airport (large wind barbs at YMOR southwest of Brisbane and YBBN northeast of Brisbane in Fig. 2), which equates to marginally supercell-supporting 0–6-km bulk wind magnitude differences of 15–20 m s^{-1} at 2300 UTC (e.g., Fig. 8 in Thompson et al. 2003). As indicated by the 0530 UTC Aircraft Meteorological Data Relay (AMDAR) sounding plotted in Fig. 4, the 0–6-km shear increased toward the late afternoon at Brisbane airport as low-level winds began to veer and strengthen below a marginally strengthening westerly midlevel flow.

3. Data and methodology

This section outlines the observational datasets used to analyze the event. Two S-band Doppler radars, CP2 and Mount Stapylton (see Fig. 5 for their location) provided complementing views of the storm. CP2 is a dual-wavelength (X and S bands), polarimetric research radar operated by the Centre for Australian Weather and Climate Research (CAWCR). CP2 (S band) is operated with a 0.93° beam at a wavelength of 10.7 cm with 150-m-range resolution. CP2 commonly scans every 6 min with a maximum range of 142.35 km, and the Nyquist velocity of the radar is 27.2 m s^{-1}. More details can be found in Keenan et al. (2007),

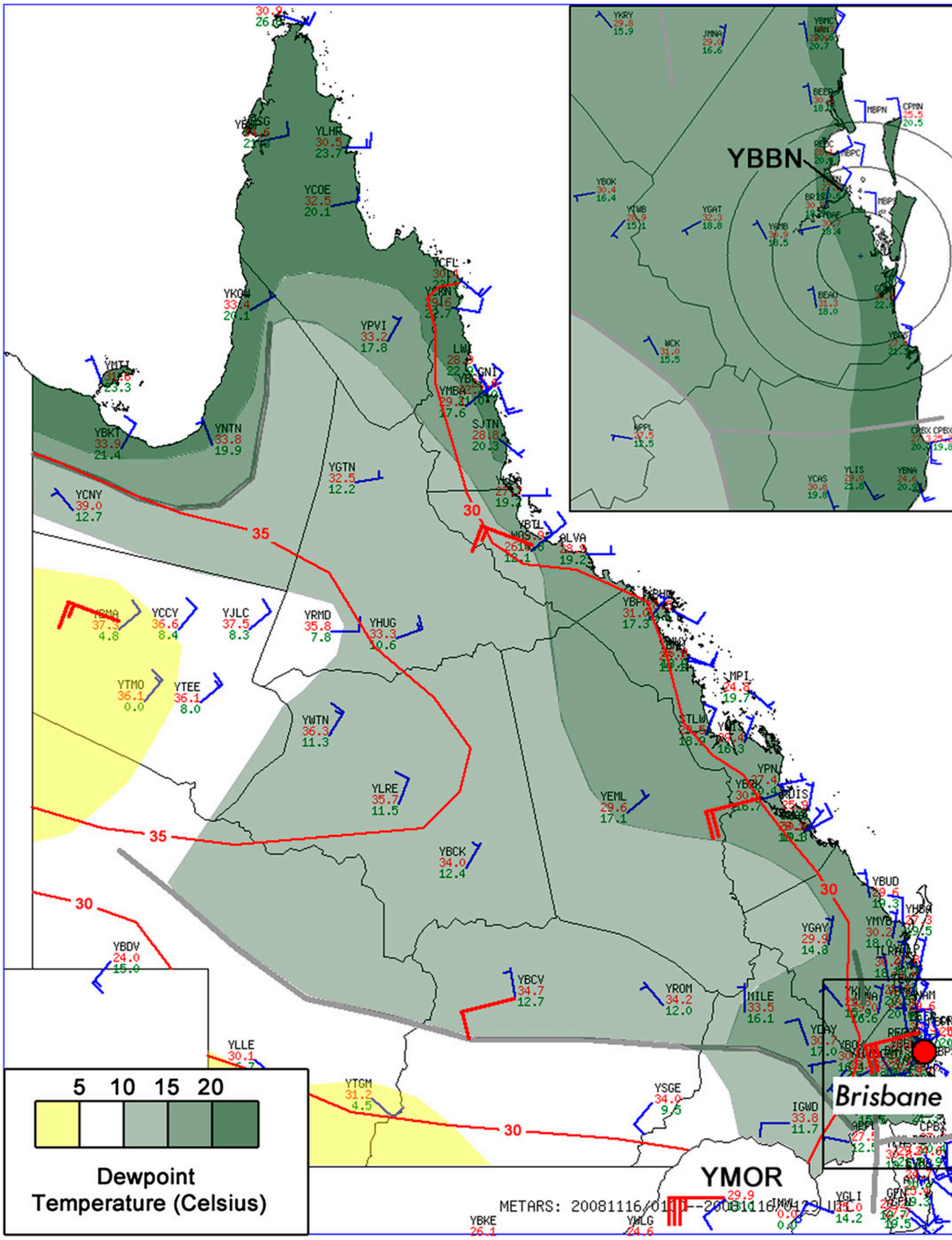

FIG. 2. The observed surface dewpoints (in °C, shaded in green), surface winds (short barb, 2.5 m s^{-1}; long barb, 5 m s^{-1}), and surface temperatures (also in °C, red solid contours) at 0100 UTC 16 Nov 2008 across QLD. The observed 500-hPa winds at radiosonde locations are overlaid using larger red wind barbs (otherwise following the same notation as for the surface winds). The thick gray line segments mark surface airmass boundaries. The inset in the top-right corner magnifies the area surrounding Brisbane (and omits the surface temperature analysis). The circles in the inset mark the 25-, 50-, and 75-km radar range rings for the Mount Stapylton radar south of Brisbane. All analyses are subjective.

Bringi and Hendry (1990), and Keeler et al. (1984; 1989). Mount Stapylton is an operational radar of 1° beamwidth with a range resolution of 250 m and a temporal resolution of 6 min.

The data accuracy of CP2 has been verified through extensive comparisons of radar-based rainfall estimates with rain gauge and video disdrometer measurements (Pepler and May 2012), as well as with a recent calibration

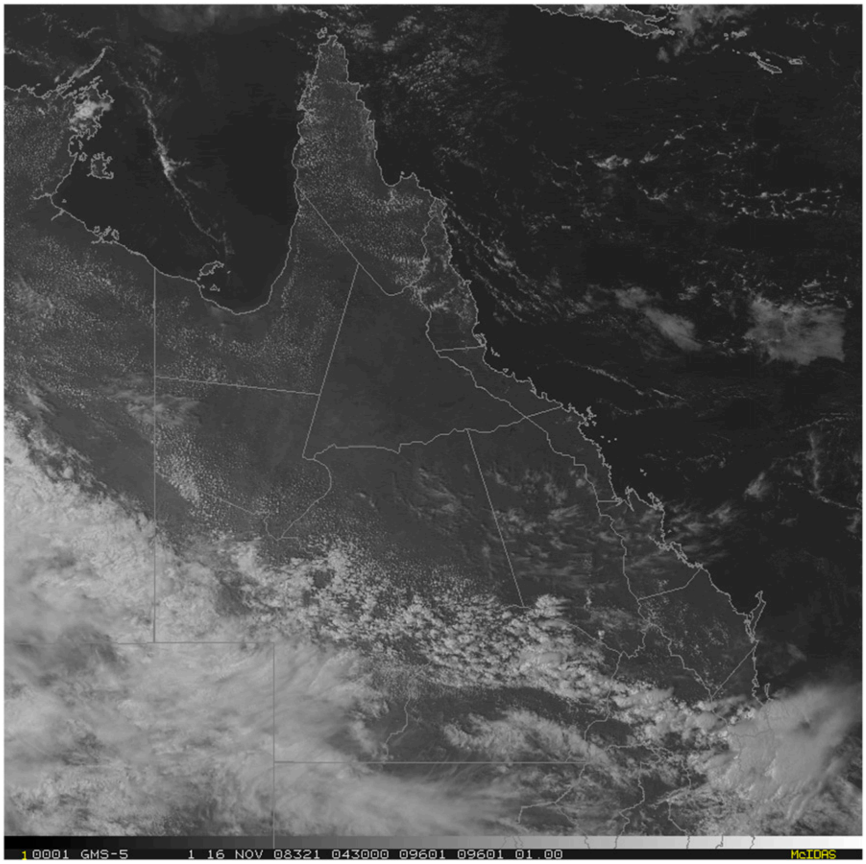

FIG. 3. *GMS-5* VIS image at 0430 UTC (base scan) 16 Nov 2008. The main trough analyzed in Fig. 1 is clearly marked by deep convection throughout most of QLD.

45–51 days prior to the Gap storm (K. Glasson 2013, personal communication).

In addition to the radar data, upper-air information from YBBN soundings (including AMDAR) was used, and surface observations were obtained from Automatic Weather Stations (AWSs) operated by the Bureau of Meteorology in Australia. *Geostationary Meteorological Satellite-5* (*GMS-5*) images are provided to the bureau by the Japan Meteorological Agency (JMA).

4. The Gap storm initiation and intensification

A closer inspection of the event indicates that mesoscale boundaries were a likely contributor to the storm's behavior and possibly the storm's intensity. The boundaries in this section were identified as temporally and spatially coherent radar finelines in the lowest few scan elevation angles.

At 0442 UTC a north–south-oriented sea-breeze front (SBF) intersected a northward-moving front–outflow boundary east-southeast of Harrisville (Figs. 5 and 6a). The future Gap storm initiated near this triple point (Kingsmill 1995) after 0500 UTC and by 0530 UTC became uniquely identifiable as an intermittently rotating elevated storm east of Harrisville ~20 km south of the cold front by 0530 UTC as part of a broken line segment of severe storms (locations shown in Fig. 5). By 0540 UTC the storms had turned left to propagate almost due north, consistent with the preferred new updraft growth on the left flank of an existing persistent and strong updraft in an environment characterized by a counterclockwise-turning hodograph (Rotunno and Klemp 1982, 1985).

Between 0548 and 0624 UTC, the northward advance of the cold front stalled over The Gap and Brisbane City, while the same boundary continued to move north farther to the west of The Gap and into the meridionally aligned valley of the Brisbane River in which the town of Esk is located (Fig. 5). In addition to the northward funneling of the cooler air through the Brisbane River valley, one plausible explanation for this differential northward advance of the front around 0600 UTC is that postfrontal surface pressure falls associated with the by now very large Gap storm (with storm-scale rotation in the midlevels)

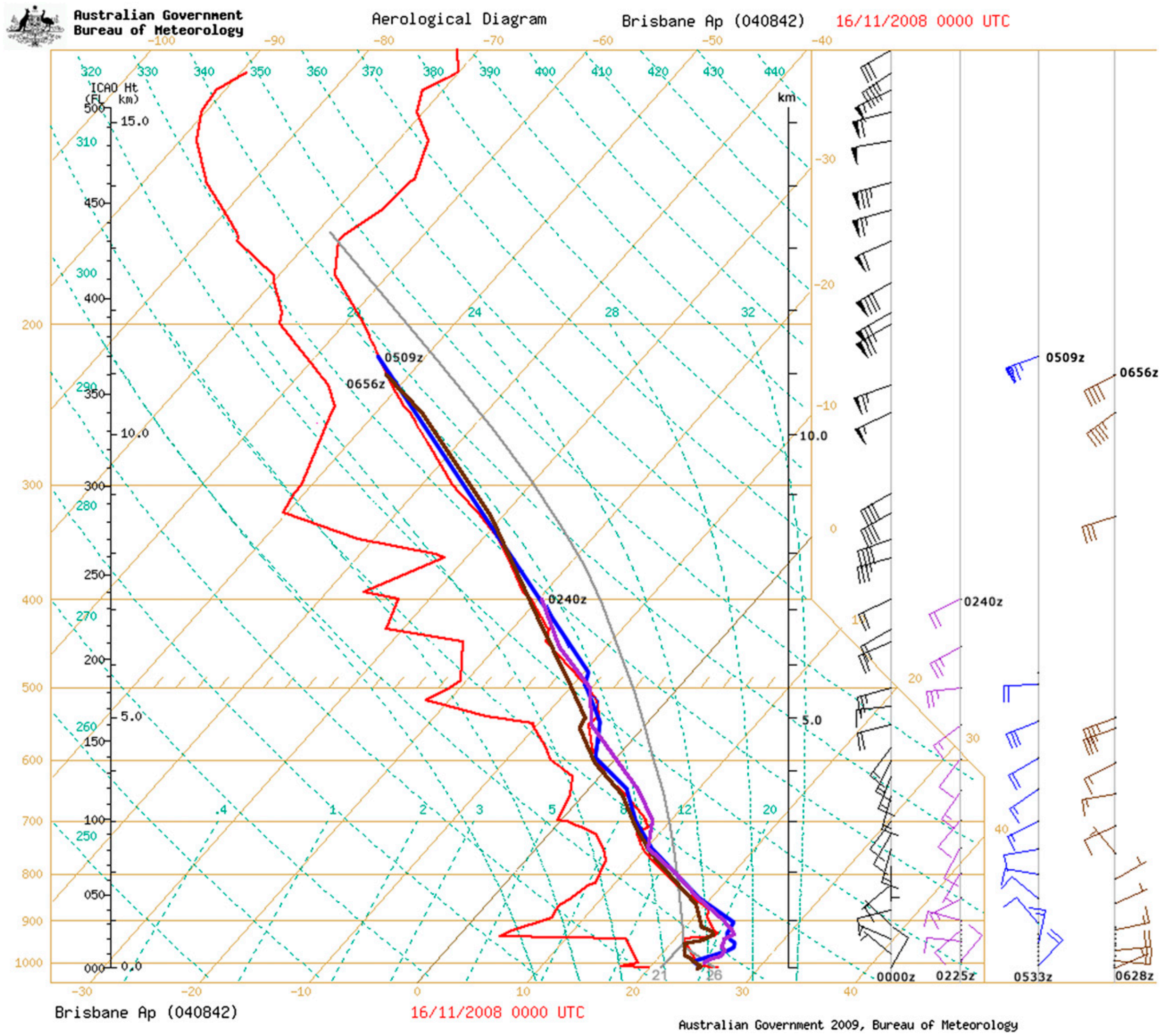

FIG. 4. Regular 0000 UTC 16 Nov 2008 sounding from the Brisbane airport (red) alongside AMDAR reports of thermal and wind profiles at 0225 (purple), 0533 (blue), and 0628 UTC (brown). Note that the 0533 UTC profile was taken by an incoming aircraft from the west-northwest (passing less than 10 km to the north of The Gap), whereas the 0628 UTC sounding was sampled by the same aircraft departing to the north-northeast, which took the plane out to sea shortly after takeoff. The ascent trajectory of a maximum energy 26°/21°C surface parcel (based on the observed 26.3°/20.6°C surface parcel southeast of The Gap in Fig. 6) is shown in gray. The CAPE value of this parcel when released into the 0000 UTC Brisbane airport sounding is 1541 J kg^{-1}.

east of Amberley were responsible for the stalling boundary segment to the storm's north. The stalled frontal boundary and the largely northward propagation of the Gap storm allowed its north-facing updraft to "catch up" with the boundary by approximately 0624 UTC, ~10–20 min prior to the onset of the destructive winds at The Gap.

By 0630 UTC, the Gap storm was the eastern member in a pair of large storms and was now fully surface-based, and quickly organized into a very compact intense multicell–HP supercell (Moller et al. 1990) by the time of the wind event at The Gap. The HP classification can be based on the storm's intermittent display of deep rotation in the 0630 and 0636 UTC base scans from the Mount Stapylton radar (rotational velocities around 15 m s^{-1} over a depth of 3–4 km) in combination with other attributes such as a bounded weak echo region (BWER) between 0624 and 0642 UTC, maximum reflectivity values exceeding 70 dBZ, and a storm motion vector deviating substantially to the left of the deep-layer mean flow.

Four air masses could be identified at 0612 UTC, about 20 min before the onset of the destructive surface winds

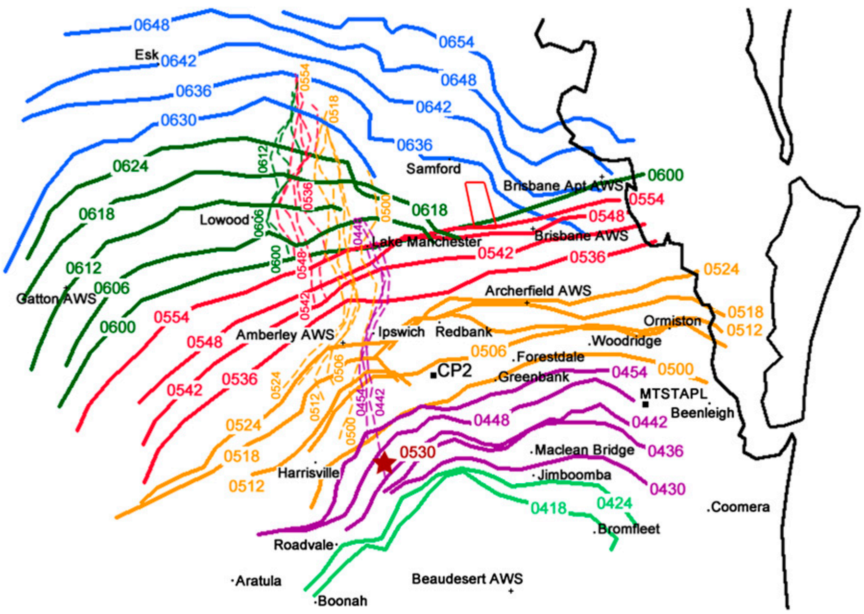

FIG. 5. Isochrones (labeled with UTC times) of the southerly cold front–dominant cold pool edge moving north (solid lines), and a sea-breeze front moving west (dashed lines) during the afternoon of 16 Nov 2008. For improved discernibility of the boundary movement, the boundaries have been grouped into half-hourly bins color coded in light green (before 0430 UTC), purple (0430–0500 UTC), mustard (0500–0530 UTC), red (0530–0600 UTC), green (0600–0630 UTC), and blue (after 0630 UTC). Note that the 0530 UTC scan from CP2 is missing. The star symbol east of Harrisville marks the location of the Gap storm shortly after initiation at 0530 UTC.

over The Gap: a more continental hot and moderately humid air mass (quadrant I), a more maritime humid and warm air mass in which The Gap resided (quadrant II), a cool and moist postgust front air mass (quadrant III), and farther inland a cool and slightly less moist postfrontal air mass (quadrant IV; Fig. 6b). The updrafts associated with the destructive winds at The Gap appear to source most of their boundary layer inflow from quadrant II, although the actual destructive winds after 0630 UTC occurred within quadrant III with ~22°/21°C (temperature/dewpoint temperature) parcels at the surface. Insertion of a 26°/21°C surface parcel (representing the inflow in quadrant II) into the 2300 UTC 15 November 2008 Brisbane airport sounding (Fig. 4) shows a very low lifted condensation level (LCL) of ~950 hPa, 81 J kg^{-1} of convective inhibition (CIN), a level of free convection (LFC) at ~820 hPa, and surface-based convective available potential energy (SBCAPE) of only 1541 J kg^{-1}. Note that the 0000 UTC temperature profile above the boundary layer remained quite similar to the AMDAR temperature profiles later in the day.

5. Discussion of potential causes of the destructive surface winds

In this section we will present a variety of separate physical mechanisms that, in aggregate, can explain the ferocity of the observed surface winds at The Gap on 16 November 2008. Apart from more commonly studied downdraft forcings such as the evaporation of liquid water, the often-neglected downward drag from the descent of a large and intense elevated hail core associated with rapid updraft weakening was likely to have been an appreciable contributor to the observed destructive surface winds as a detailed quantitative estimate of the drag forcing will show. More importantly, the very strong near-surface winds within the Gap storm's outflow were most likely the result of near-ground horizontal accelerations from the cold pool into a storm-scale low associated with a low-level circulation.

a. Intensity of the maximum surface winds

The previously stated peak radial velocity of 43 m s^{-1} is the result of a *subjective* correction to the "raw" maximum value of 49 m s^{-1} returned by the CP2 radar. A radial cross section through the radial velocity maximum at 0648 UTC shows the peak radial velocity of 49 m s^{-1} (Fig. 7). A range of factors cast doubt on the accuracy of this single pixel peak value. The raw radial velocity data imply a bin-to-bin radial parcel acceleration of 10 m s^{-1} over a distance of ~150 m, and a range of other unrepresentative radial velocity pixels are present on the mesoscale. Further, the CP2 radar beam took samples at

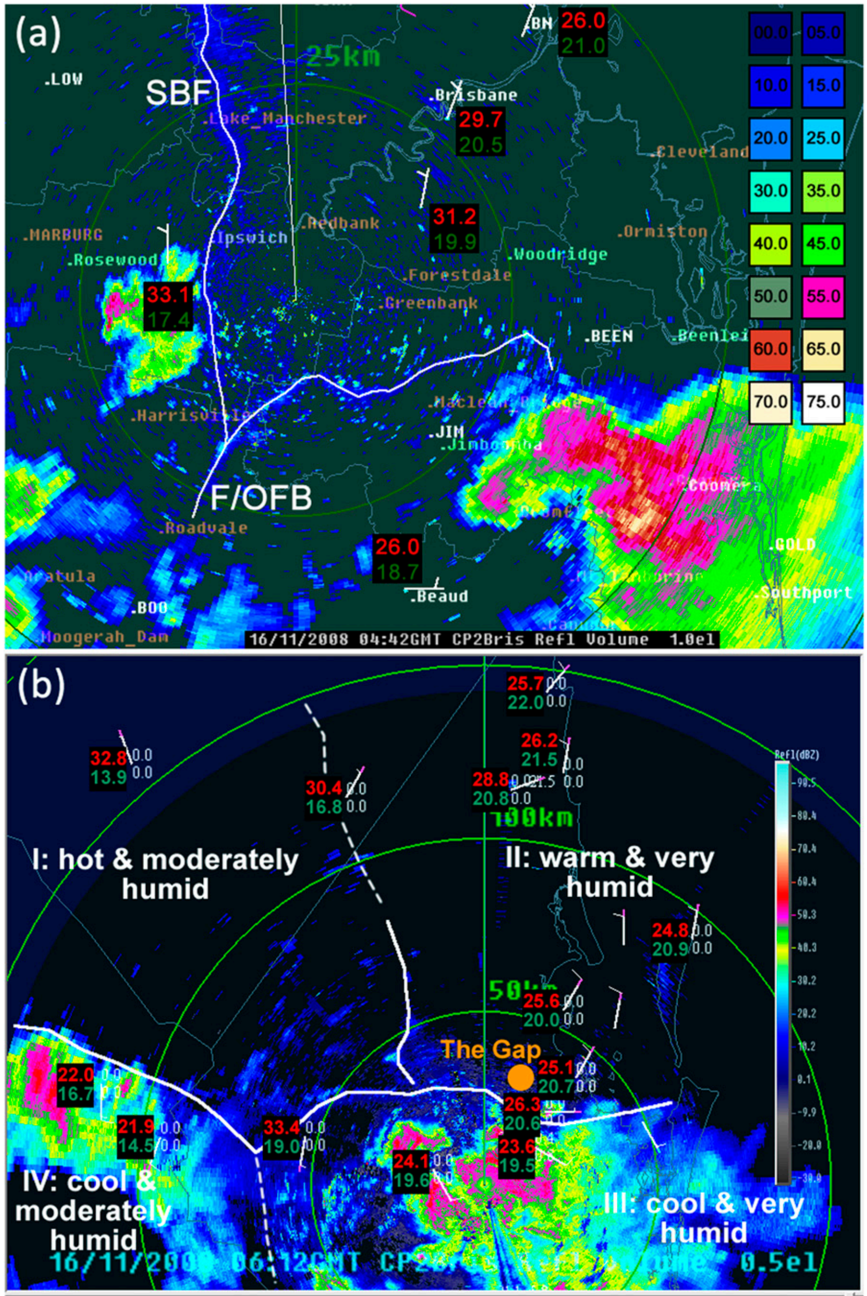

FIG. 6. (a) Mesoscale surface analysis at 0442 UTC 16 Nov 2008, around the time of the demise of the initial supercell visible in the southeastern corner of this plot, and ~45 min prior to the initiation of the Gap storm. The airmass boundaries were drawn based on radar reflectivity finelines; the front–outflow boundary moving north is marked F/OFB, and the westward-moving sea-breeze front is marked SBF. All surface winds show flow of magnitude 2.5 m s^{-1} (half barb), with both surface temperatures (in red) and dewpoint temperatures (in green) given in °C. Underlaid is the 1° tilt base reflectivity image from the CP2 radar. (b) Mesoscale surface analysis at 0612 UTC 16 Nov 2008, approximately 30 min before the onset of the destructive winds at The Gap. The solid white lines mark clearly identifiable sections of the F/OFG and SBF, and the dashed white lines mark sections identified with lower confidence.

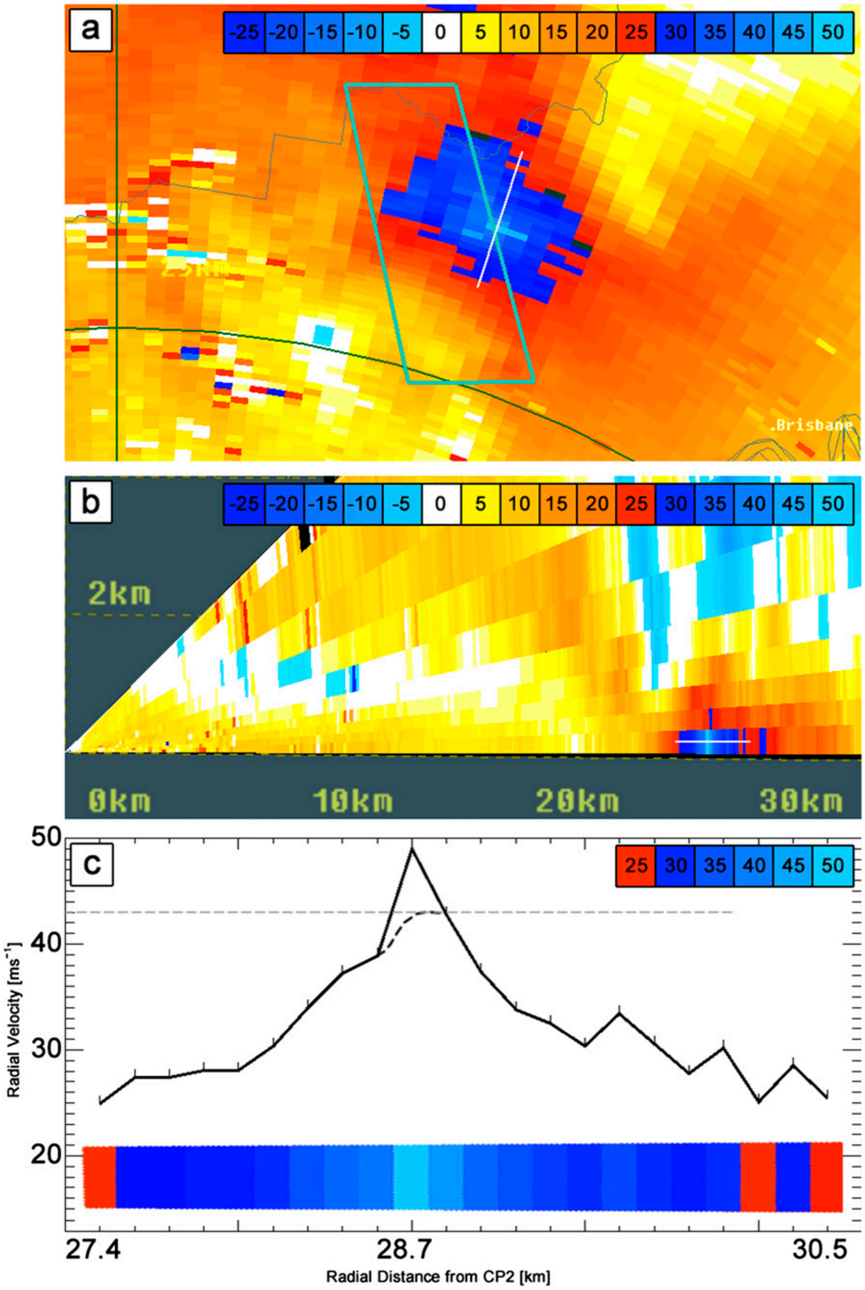

FIG. 7. (a) Radial velocity on the 0.5° plan position indicator (PPI) scan of the CP2 radar at the peak of the Gap storm wind event (0648 UTC). The blue colors along the eastern border of the wind damage polygon in (a) are aliased values where the radial velocities exceed the radar's Nyquist velocity of 27.2 m s^{-1}. (b) Vertical cross section through the peak aliased velocity in (a) at a distance r from the CP2 radar (in km) along the radial axis, and height above the mean sea level along the vertical axis. (c) Unaliased radial velocity profile along the radial segment [shown by white lines in (a) and (b)]. The uncorrected peak radial velocity of 49 m s^{-1} occurs at r = 28.7 km. Color bar radial velocities are in m s^{-1} and are negative for inbound velocities and positive for outbound velocities.

466 m (the beam-height estimate is based on a standard atmosphere) in the presence of hills surrounding The Gap reaching almost 300 m in height. Finally, the velocity data possess a high local spectrum width value of 6.3 m s^{-1}.

For the estimation of the peak radial velocity along the 0.5° beam we treat the 49 m s^{-1} value as a missing value and fit a cubic polynomial to the two adjacent radial velocity measurements on either side. This interpolation is

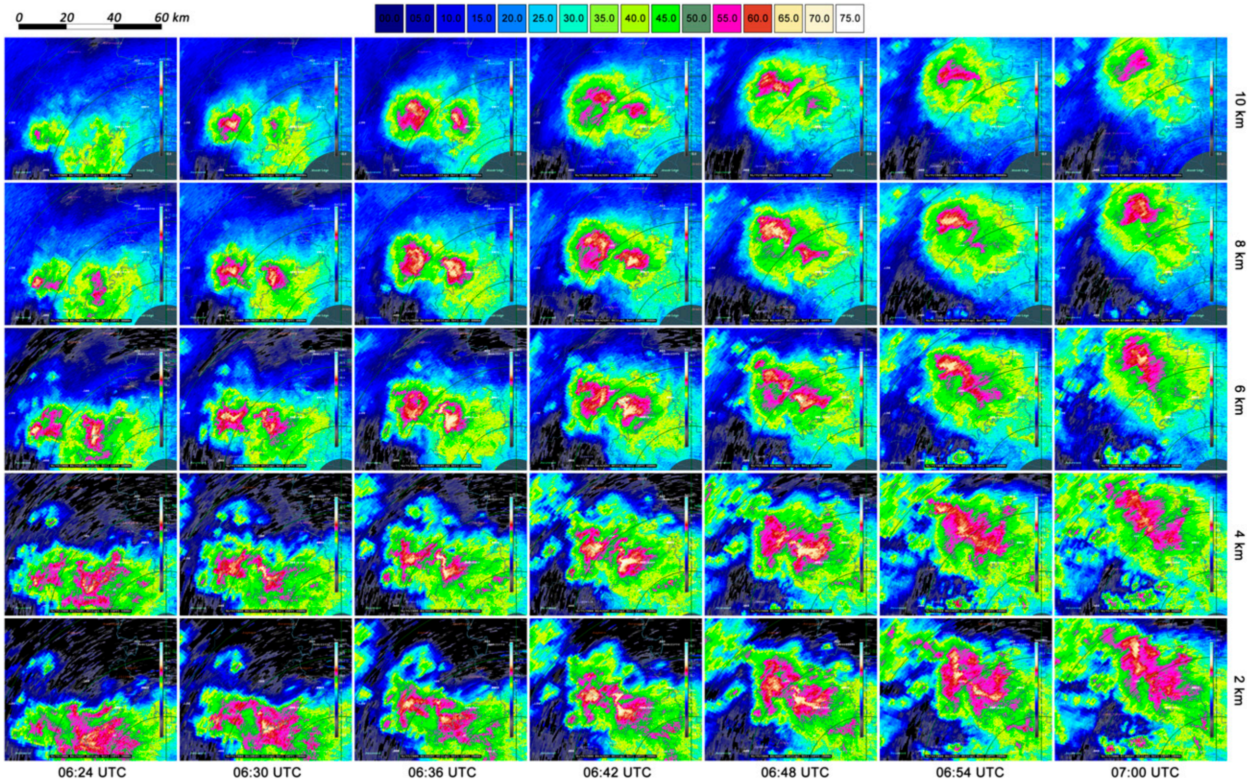

FIG. 8. Mount Stapylton radar CAPPIs at heights of 2, 4, 6, 8, and 10 km (from bottom row to top row) for base scan times from 0624 (leftmost column) to 0700 UTC (rightmost column) in 6-min time steps.

shown as a dashed curve in Fig. 7c and produces a corrected radial velocity maximum of 43 m s^{-1}, which is also a closer match to the inferred 10-m peak gust value of 45 m s^{-1} derived from a postevent damage assessment (Leitch et al. 2009, p. 26).

b. *Thermodynamic downdraft drivers of the Gap event as a wet microburst*

1) ELEVATED CORE OF LARGE HAIL

A time series of constant-altitude base reflectivity images across various heights indicates that the Gap wind event was preceded by a large and intense reflectivity core descending from the upper levels of the storm to the surface. Figure 8 shows that at 0636 UTC the Gap storm possessed its most intense core aloft ($z \geq 6$ km). The updraft displayed a BWER (Phillips 1973) at $z =$ 6 km as an indicator that the storm was strong at this time. After 0636 UTC the upper-level core at $z = 10$ km began to decrease in reflectivity, while the cores at lower altitudes (between $z = 2$ and 4 km) reached their peak reflectivity in the subsequent two radar scans at 0642 and 0648 UTC. This behavior suggests a descending hail core as a key player in the generation of the strong surface winds.

The storm's large core at 0636 UTC contained peak reflectivity values exceeding 70 dBZ (on CP2 and Mount Stapylton) at that height where ambient temperatures measured −15°C. Despite the large reflectivity values present in the hail growth zone (from −10° to −30°C), it is likely that the Gap storm contained a large mass of hailstones below giant size (≥102 mm in diameter). Blair et al. (2011) found that 75% of giant-hail-producing storms (based on their *Storm Data* sample) contained midlevel mesocyclones with rotational velocities exceeding 20 m s^{-1} and storm-top divergence magnitudes exceeding 60 m s^{-1}. Also, 99% of their giant-hail-producing storms were supercells. In contrast, the Gap storm only showed intermittent midlevel rotation while reaching a maximum rotational velocity of ~17 m s^{-1} and a storm-top divergence magnitude of ~53 m s^{-1}.

Additional evidence that a descending hail core was instrumental in the Gap windstorm comes from some of the polarimetric variables observed by CP2. Figures 9a and 9b show the collocation of a 70-dBZ reflectivity core with a patch of near-zero differential reflectivity Z_{DR} at 0630 UTC about 7–8 km AGL (with an ambient temperature between −18° and −27°C; see Fig. 4). At 0642 UTC a similar combination of high (horizontal) reflectivity Z_H and low Z_{DR} was observed very close to and

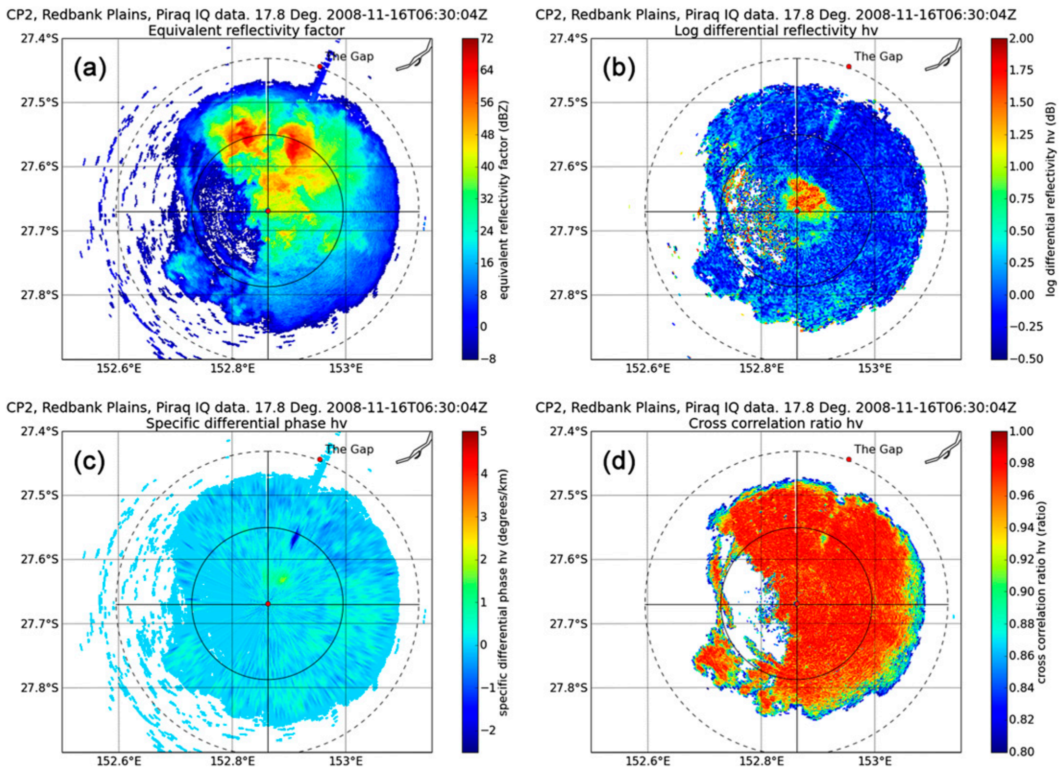

FIG. 9. A 17.8° PPI image of (a) Z_H, (b) Z_{DR}, (c) K_{DP}, and (d) ρ_{hv} as observed in the 0630 UTC base scan by CP2 (located at the origin). The location of The Gap is denoted by a red circle north-northeast of the radar origin. At the Gap storm location the radar beam is approximately 6 km AGL. There is also a TBSS to the north-northeast of the radar.

approximately 600 m above the damage area at The Gap (Fig. 10). Wakimoto and Bringi (1988), among others, previously documented that a low-Z_{DR} column inside a high-reflectivity core is likely to be indicative of a hail shaft and, in their case, was also associated with a microburst generated by a thunderstorm in northern Alabama. Even nonspherical hailstones tend to produce low-Z_{DR} returns because they tumble and rotate on descent and their orientation is generally characterized by a relatively wide distribution of canting angles; that is, they are statistically isotropic scatterers. Finally, Fig. 9 shows streaks of high positive Z_{DR} down radial of, and negative specific differential phase K_{DP} with low values (~0.9) of, the correlation coefficient ρ_{hv} collocated with the storm's core. This is suggestive of a mixture of hail and more vertically oriented low inertia ice crystals in the presence of the storm's electrostatic field (Hubbert et al. 2014). The absence of a positive Z_{DR} or K_{DP} signal indicates that there are no large oblate liquid state scatterers (such as large raindrops) present (Zrnić et al. 1993; Ryzhkov and Zrnić 2007).

The Gap damage area closely matched the observed low-level hail-core swath as seen from the Mount Stapylton radar. Figures 11 and 12 show that the Gap storm first produced a more substantial low-level core exceeding 62 dBZ in the 0.5° scan at 0642 UTC, just south of the wind damage report area at The Gap. The intense low-level core lasted for three scans, with no further returns in excess of 62 dBZ after 0654 UTC, at which time the core had concluded its descent in the northern parts of the damage area. The timing of the onset and demise of the low-level hail core and its track through precisely the damage area strongly suggest that it was instrumental in the destructive wind event.

The apparent initial descent of the hail core south of the damage area should be put into perspective. This area is sparsely populated, forested and hilly bushland that is unlikely to generate numerous damage reports due to the lack of infrastructure. One of the few buildings in the area (the Channel 7 building on Mount Coot-Tha) did suffer roof damage (Brisbane Regional Forecasting Centre 2013, personal communication). Extensive tree damage has also been documented in this area (Leitch et al. 2009).

The threshold of 62 dBZ has been subjectively chosen as this value best illustrated the progression of the low-level

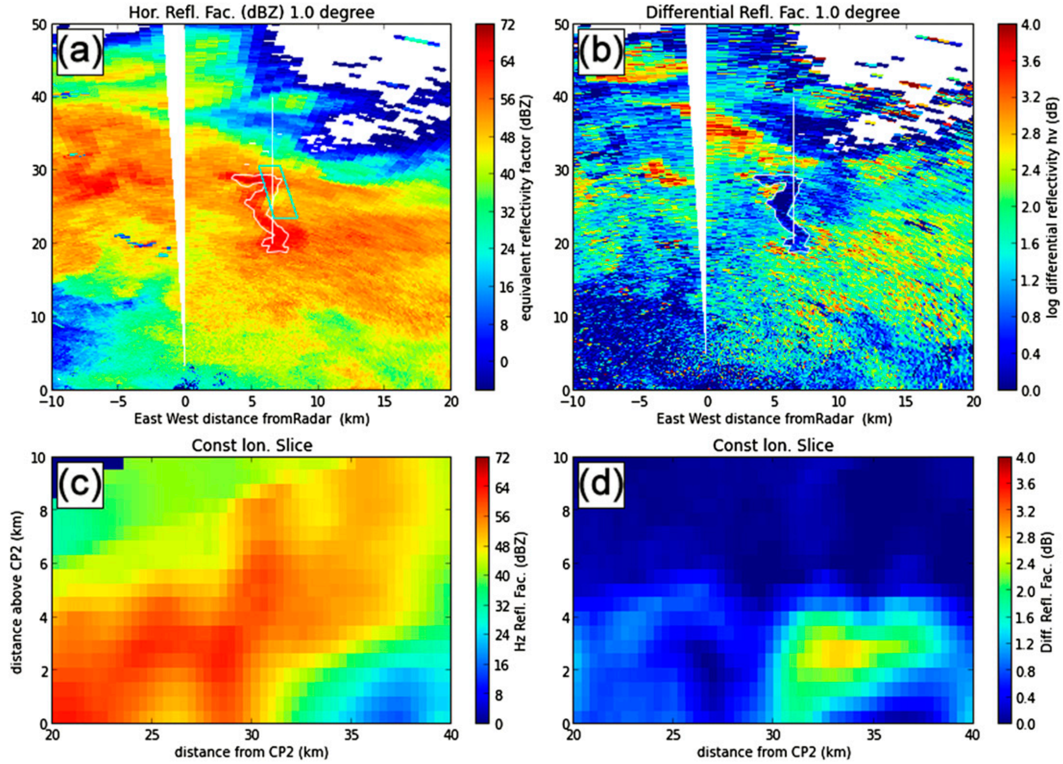

FIG. 10. (top) A 1° PPI scan of (a) the horizontal reflectivity factor Z_H and (b) the differential reflectivity Z_{DR} as seen by the CP2 radar at 0642 UTC. (bottom) Corresponding vertical cross sections through (c) Z_H and (d) Z_{DR} along a 20-km north–south-oriented segment marked by a white line in the top panels. The Gap damage area is shown as a turquoise polygon in (a). The irregular white outlines in (a) and (b) indicate distinct areas of low Z_{DR}.

hail core without generating numerous isolated "pixels" in Fig. 12. Lemon (1998) associated reflectivity returns of 63 dBZ or higher in conjunction with a ≥5-dBZ three-body scatter spike (TBSS) signature as seen by S-band radars with severe hail observations on the ground (Lindley and Lemon 2007). Such a TBSS can also be seen on several occasions in the Gap storm (e.g., Fig. 9 shows a TBSS exceeding 10 dBZ).

These indicators, in combination with observations of golf-ball-sized hail after prolific melting (see below), suggest that there was a large amount of significant hail present in the upper parts of the Gap storm prior to the wind event. We will now explore why the storm environment was thermodynamically favorable for responding to a descending core of large hail with the very strong observed surface winds.

2) High melting level

Figure 13 indicates that the descending hail would have begun to melt at around the wet-bulb zero level of ~3740 m AGL (The Gap is located 56 m above sea level). The most representative thermal profile in the lowest few kilometers experienced by the Gap storm just prior to the damaging surface winds was sampled by the 0533 UTC AMDAR sounding. Although the 0628 UTC AMDAR profile might appear to be better suited for the description of the storm environment, the profiling aircraft left Brisbane airport in a northerly direction over the sea (Fig. 14), which led to the sampling of the less representative offshore marine boundary layer with distinctly cooler low-level temperatures and low-level winds influenced by the land–sea temperature contrast (Fig. 4).

3) Dry-adiabatic lapse rates and dry air below the melting level

A nearly 3-km-deep layer of steep lapse rates extends from the melting level around 3.74 km downward toward 1 km AGL (900 hPa), with the lower portion (900–750 hPa) approaching dry-adiabatic lapse rates. Ryzhkov et al. (2013), using a thermodynamic profile broadly comparable to the 16 November 2008 Brisbane airport sounding at 0000 UTC (Fig. 4), showed that melting of 25–35-mm-diameter hailstones reduces the effective ice-core diameter only by about 5 mm on the way to the surface, while stones with initial diameters below 14 mm

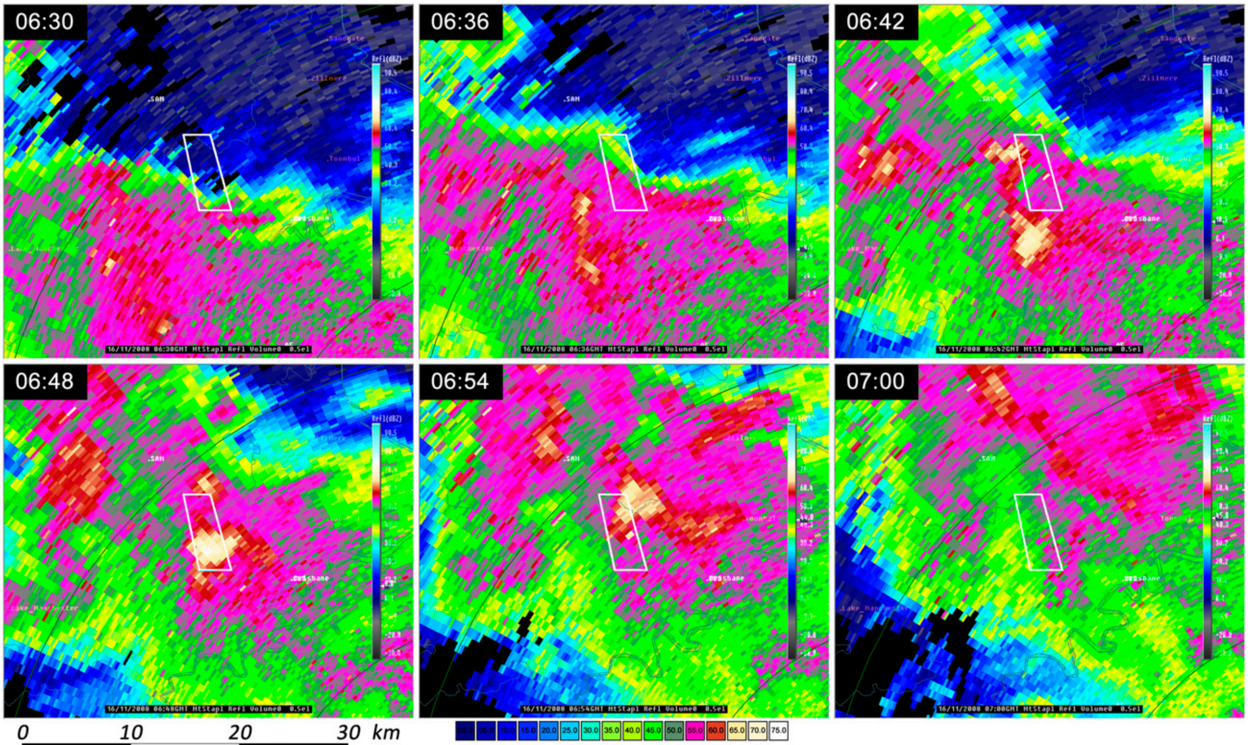

FIG. 11. Mount Stapylton radar base reflectivity scans at 0.5° elevation during a time where a low-level hail core traversed the damage area of the Gap storm (white polygon). The color bar shows base reflectivity values in dBZ.

melt entirely. With reported hail sizes not exceeding golf-ball size, this finding suggests that the maximum initial hail sizes in the Gap storm were not significantly larger than golf balls.

Figure 13 also shows that the ambient air between ~930 and 800 hPa is relatively dry, allowing the meltwater to efficiently evaporate so that the developing downdraft is cooled through two separate diabatic processes. P89 also identified dry air around the melting level as conducive to downdraft acceleration as it allows entrainment of dry air and evaporative cooling right where the liquid first becomes available. This process, however, also reduces the hail melting rate (Ryzhkov et al. 2013). Due to the dry-adiabatic lapse rates, the downdraft likely remained negatively buoyant below the melting level and accelerated until it reached the 900-hPa level, about 1 km above the ground.

Above 900 hPa, the 0533 UTC sounding (assuming the 0000 UTC 16 November 2008 moisture profile is still representative of the 0533 UTC conditions) is reasonably similar to the baseline simulation in P89 characterized by the 2300 UTC 30 June 1982 Denver, Colorado, sounding. In both cases the ambient melting level was located around 3 km above the base of a dry-adiabatic layer in the presence of dry air. P89 found that a wet microburst containing a descending hail core experienced significant cooling only after the hail core had descended through a ~2-km-deep dry-adiabatic subcloud layer below the melting level. For a 71-dBZ core [assuming an exponential hail size distribution following Lin et al. (1983)], P89 simulated an 11°C temperature deficit in the cold pool and a maximum downdraft speed of 19.4 m s^{-1} suggestive of a strong thermodynamically forced downdraft impacting the top of the near-surface stable layer in the Gap storm case.

c. *Downdraft forcing due to very large condensate loading*

Prompted by the large radar reflectivity located above the freezing level and indications that large amounts of hail were present in the Gap storm (see section 5b above), we now examine more closely how hail loading aloft might influence the downdraft speeds above The Gap. The integration of the Boussinesq form of the vertical momentum equation for a standard atmosphere where the downdraft is driven only by the hail-loading term results in an analytical solution for the downdraft speed as a function of the reflectivity Z_{dB} and initial core height z_i (Fig. 15; see the derivation in the appendix). For reflectivity values of 60 dBZ or less, even hail-driven

FIG. 12. Schematic highlighting the time evolution of the >62-dBZ low-level reflectivity core of the Gap storm between 0630 and 0706 UTC 16 Nov 2008 in the 0.5° scan of the Mount Stapylton radar. The time of occurrence of the 0.5° core is color coded. The vast majority of the wind damage reports were clustered inside the black polygon.

downdrafts with a very high origin height of 10 km do not exceed downward velocities of 25 m s^{-1}. As the hail-core reflectivity is increased from 60 to 70 dBZ, the downdraft strength nearly doubles to 50 m s^{-1} for a parcel descent from z_i = 10 km. This increasing sensitivity of downdraft strength to the underlying core intensity with increasing Z_{dB} is not too surprising, given the nonlinear increase in the hail mixing ratio with Z_{dB} ($q_H \sim 10^{Z_{\mathrm{dB}}/17.5}$) and the linear relationship between the downdraft acceleration and the hail mixing ratio [see the appendix, Eqs. (A1) and (A3)].

A simple comparison of the relative importance of downdraft cooling through evaporation and the equivalent "cooling" due to hydrometeor loading suggests that the cooling potential due to evaporation of liquid water is nearly one order of magnitude (8.3 times) larger (Wakimoto 2001, p. 260). The melting of ice would further augment this cooling potential imbalance because of the additional contribution of the latent heat of fusion. However, there are two considerations that need to be kept in mind in this comparison. First, in any wet microburst where the melting of ice or the evaporation of water is incomplete, only a fraction of the potential cooling effect due to phase changes is realized. With hail up to golf-ball size and heavy rain reported in the Gap storm downdraft, this first consideration seems to be applicable to this event. Second, even with condensate loading being a minor partner in the downdraft forcing, the results above suggest that for intense hail cores with reflectivities exceeding 60 dBZ, the hail-loading term appreciably contributes to the downward acceleration of air parcels in the downdraft as revealed by the sensitive nonlinear relationship between reflectivity and the hail mixing ratio.

The final downdraft velocities in Fig. 15 also require some qualifications. The assumption was made that the hail-mixing ratio was constant through the descent of a downdraft parcel from an initial level to the ground (other than changes due to increasing ambient air density). In reality, hailstones melt below the melting level and the downward forcing due to hail loading would decrease over time once the downdraft parcel resides below the melting level. In addition, the downdraft decelerates near the ground as it starts to interact with the storm's cold pool. For these two reasons alone the vertical velocity magnitudes in Fig. 15 are an overestimate of realistic near-ground downdraft speeds.

d. Horizontal acceleration of the outflow due to thermodynamic processes

P89 showed for the baseline case (the 2300 UTC 30 June 1982 Denver sounding) that a wet microburst containing hail experienced significant cooling only in the lowest kilometer of its descent through a ~2-km-deep dry-adiabatic subcloud layer below the melting level. Wakimoto (2001) pointed out that the cooling due to melting hail and the subsequent evaporation of liquid water does not necessarily enhance the vertical downdraft strength significantly, but that the *near-ground cooling strengthens the overall outflow wind speeds through an increase in the horizontal density gradient*. Despite an 11°C peak temperature drop, the maximum downdraft vertical velocity in P89 was only 12 m s^{-1} for the baseline case while the simulated surface outflow wind difference reached 42 m s^{-1} (which means outflow winds of nearly twice the magnitude of the downdraft assuming a symmetric outflow divergence pattern). Any explanation of downdraft-related *outflow winds* must therefore carefully inspect how downdraft properties influence the strength of the final near-ground horizontal flow in the cold pool.

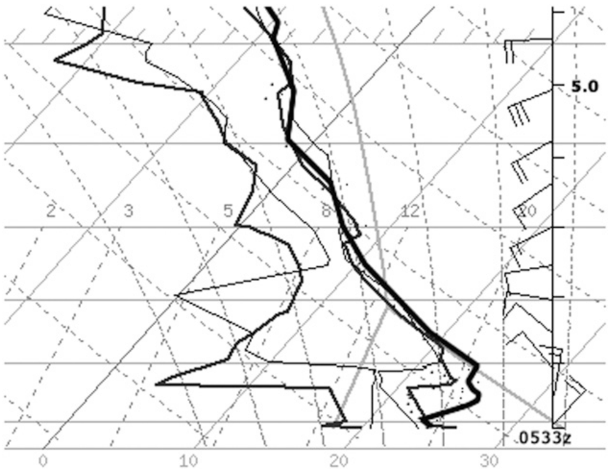

FIG. 13. Close-up version of the 0000 UTC 16 Nov 2008 Brisbane airport sounding (lines of medium thickness), the 0533 UTC 16 Nov 2008 AMDAR sounding (thick lines) with its attendant wind profile (short barbs, 2.5 m s^{-1}; long barbs, 5 m s^{-1}; vertical scale in km), and the 1200 UTC 15 Nov 2008 Brisbane airport sounding (thin lines). Tick marks on the vertical scale to the right are in km above sea level.

The vertical cross section through the core of the strong radial winds (Fig. 7b) shows that the destructive radial winds for the Gap storm event were mostly contained in the lowest 500 m above ground level. This observation is consistent with the outflow depths of 300–1000 m produced in the P89 simulations for precipitation core diameters larger than 1 km. P89 found that the outflow depth of a microburst was primarily sensitive to the low-level lapse rates (the depth tended to match the depth of any near-ground stable layer; see p. 2150 in P89) and to the precipitation core width (the wider the core, the deeper the cold pool).

The Gap storm's hail-core width was near the upper end of the range explored by P89 with the 0636 UTC hail core (>60 dB*Z*) at 7 km AGL measuring 11 km × 6 km in areal extent (Mount Stapylton radar; not shown). The 0533 UTC sounding (Fig. 13) shows a near-ground stable layer about 1 km deep. Both of these indicators are suggestive that the Gap storm's outflow was deep, perhaps as deep as ~1 km.

The combination of efficient downdraft cooling through the partial melting and evaporation of initially large hail, downdraft acceleration in a dry-adiabatic environment underneath a relatively high melting level in the presence of dry ambient air, and the likely generation of deep outflow in a stably stratified moist low-level environment have set up a relatively deep and (above the surface) cool outflow that is subject to strong horizontal acceleration.

Once the outflow interacts with the ground, the cold pool accelerates outward into less dense ambient air, with the leading edge showing similarities to a spreading *gravity current*. The gust front's propagation speed is mainly driven by the cold pool depth H and density difference $\Delta\rho$ compared to the ambient air, in accordance with the theoretical propagation speed V of a gravity current as derived in Benjamin (1968):

$$V \sim \sqrt{2gH\frac{\Delta\rho}{\rho}}, \qquad (1)$$

where ρ is the density of the cold pool air. Even if we were to ignore the findings that observed gravity currents move with a speed V closer to half the speed given by Eq. (1) (Wakimoto 2001), and if we assume that the outflow is 1 km deep, a gust front moving at the speed of the observed Gap storm winds of 43 m s^{-1} would require a 10% density change ($\Delta\rho \sim 0.1\rho$) across the cold pool boundary, far exceeding the 4% value in P89's baseline case, which produced a cold pool surface pressure perturbation of 2.63 hPa and a far greater cold pool temperature perturbation of −11.0°C. Alternatively, there would need to be an unrealistically strong normal gust-front relative flow that makes up any difference between the actual gust front propagation speed and the value of 43 m s^{-1}. These considerations cast doubt on the notion that simple gravity current propagation provides the full explanation of the observed Gap storm wind speeds. Such doubt is supported by the relatively small observed differences in surface temperature and dewpoint temperature across the outflow boundary of the Gap storm. The observed 0639 UTC Archerfield temperature and dewpoint temperature were 21.7°C inside the cold pool (Fig. 5), while the 0600 UTC preoutflow sea-breeze values at Brisbane were 26.0° and 21.0°C, respectively (Fig. 6b). The observed cold pool surface temperature deficit of 4.3°C was far smaller than the −11°C counterpart in the P89 baseline simulation, likely due to downdraft warming in the stable layer near the ground relative to the environment. While the stable layer might have produced a deeper outflow, it also accounted for a reduction in the outflow temperature deficit, and hence the potential of horizontal acceleration driven by horizontal density gradients.

e. *Horizontal outflow acceleration due to dynamic processes*

The thermodynamically induced horizontal outflow accelerations neither explain the full observed near-surface wind strength nor the anisotropy of the associated radial velocity signature. The CP2 storm-relative surface velocity divergence signature (not shown) shows only a modest storm-relative southward flow of 12 m s^{-1}

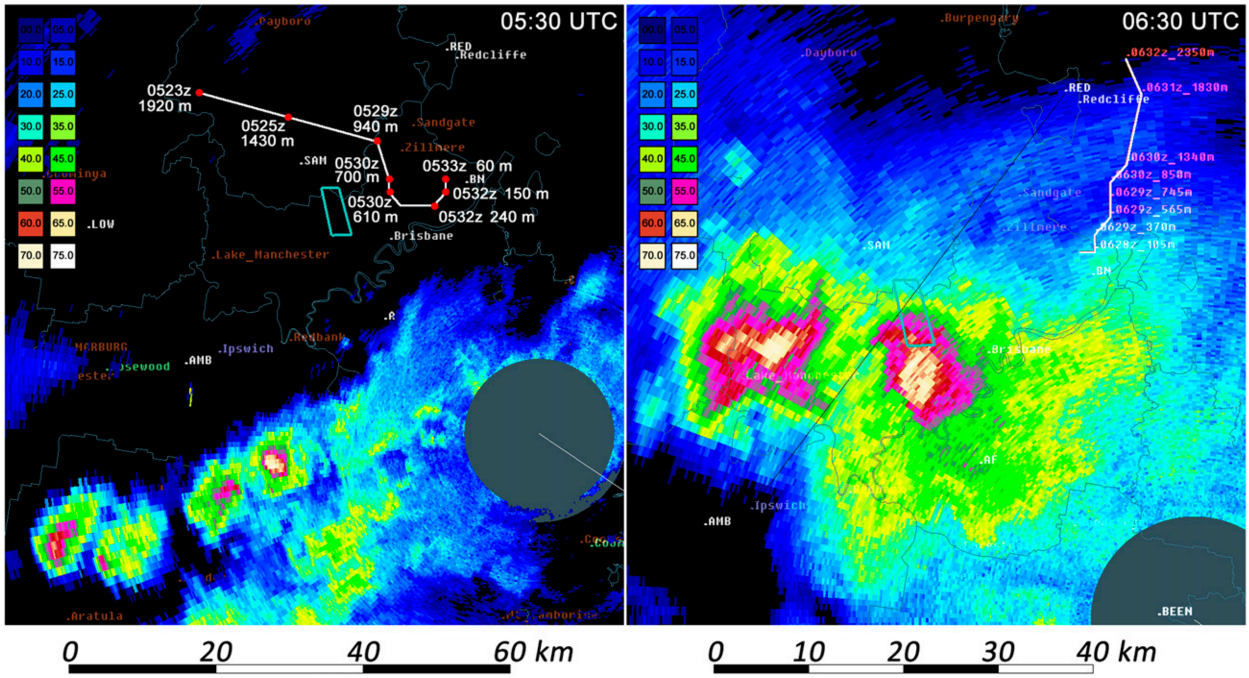

FIG. 14. Low-level flight tracks for the (left) 0533 and (right) 0628 UTC AMDAR observations. Each flight track is overplotted on the time-matching 7-km CAPPI radar image: (left) 0530 and (right) 0630 UTC. The radar images are based on observations from the Mount Stapylton radar and are of differing spatial scale to optimize the display of the actual flight track. The turquoise polygon marks the wind damage area surrounding The Gap.

or less, while the northward branch produced radial winds of 34 m s^{-1}. While the storm motion vector of 10 m s^{-1} from 200° would have augmented the north-northeast components of the outflow winds, an additional flow-accelerating forcing mechanism was probably present.

A closer inspection of the radar-observed near-surface radial wind field suggests that the full magnitude of the Gap storm surface winds received an additional dynamically driven contribution. The low-level (1.3°) storm-relative velocity scan in Fig. 16 shows a low-level circulation pattern moving in a northeasterly direction through the southern half of the Gap storm damage area (marked by a white polygon). Surprisingly, the corresponding 5.6° scans (transecting the Gap storm at around 4.6 km AGL) show that a persistent midlevel circulation was absent around the time of the maximum surface winds. This means that the Gap storm possessed a dynamically forced storm-scale perturbation low in the low levels, but not in the midlevels. Any downdraft forming above and in the vicinity of the low-level circulation in the storm would therefore have been accelerated downward toward the storm-scale low by a vertical pressure perturbation gradient acting in addition to any thermodynamic forcing already discussed (Markowski 2002). Perhaps more importantly, any thermodynamically forced downdraft descending within the neighborhood of the low-level circulation would have deposited cool outflow air close to the low perturbation pressure associated with the circulation. Conversely, at the downdraft location high perturbation pressure set up due to the composition of the hydrostatically balanced weight of the relatively cold outflow column and the dynamically induced component related to the deceleration of the downdraft near the

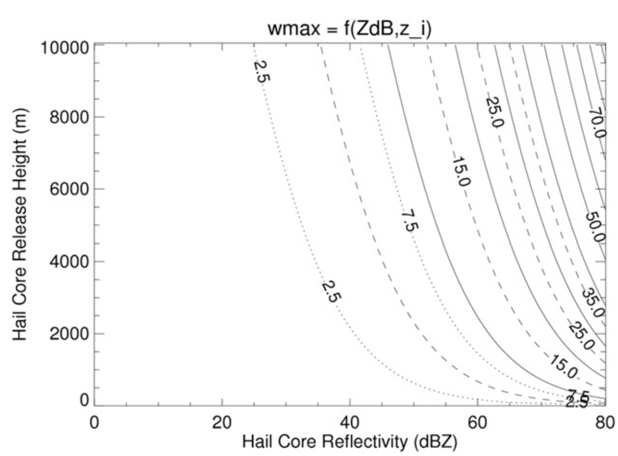

FIG. 15. Magnitude of the terminal downdraft vertical velocity w_{max} (m s^{-1}) as a function of the downdraft parcel base reflectivity (dBZ) and the altitude z_i (m) from where the parcel starts its descent. The dotted contour lines show the velocity magnitudes 2.5, 7.5 m s^{-1}, etc.; the dashed lines show 5, 15 m s^{-1}, etc.; and the solid lines show 10, 20 m s^{-1}, etc.

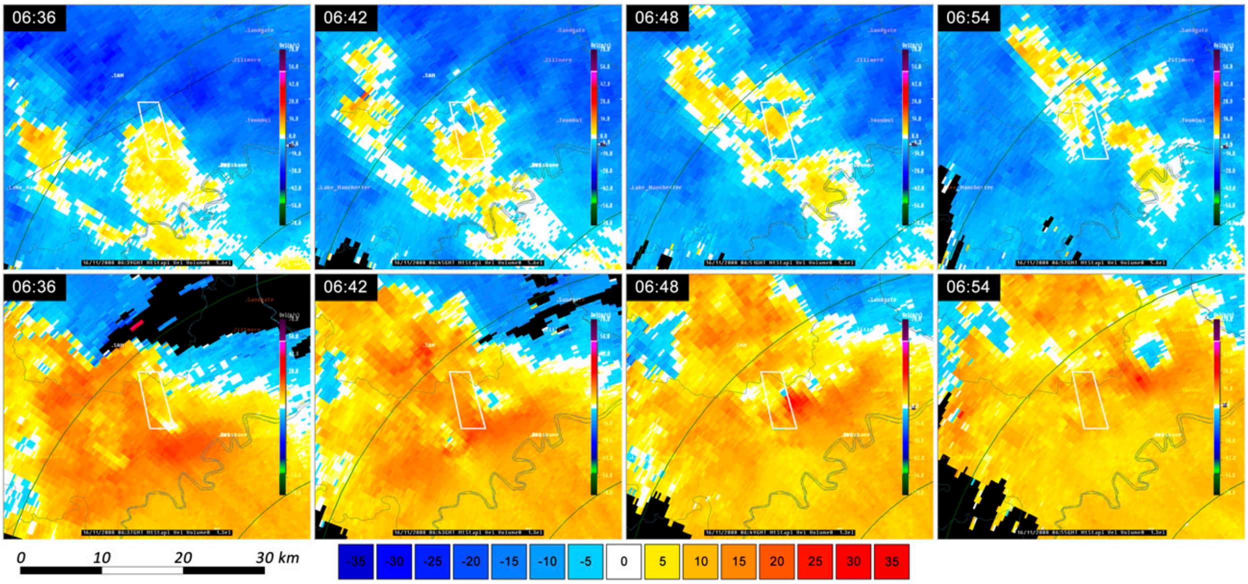

FIG. 16. Storm-relative (top) midlevel (5.6° tilt) and (bottom) low-level (1.3° tilt) velocities from the Mount Stapylton radar located beyond the bottom-right corner of each image. The two range ring segments shown are located at radii of 25 km (bottom right) and 50 km (top left). The beam center heights over the damage area are approximately 1.3 km (bottom tilt) and 4.6 km (top tilt). The white polygon marks the damage area and contains the vast majority of damage reports to the State Emergency Services.

ground. *The close proximity of the downdraft perturbation high pressure and the low-level circulation low pressure is hypothesized to have been a key driver for the horizontal acceleration of the Gap storm outflow and the magnitude of the damaging winds at the surface.* Figure 17 shows the migration of the low-level circulation and associated perturbation low across the Gap storm damage area. The maxima in the radial low-level velocities closely follow the low-level circulation center, in support of the hypothesis above. The 0630 and 0636 UTC scans in Fig. 17 also show that the storm's low-level circulation existed prior to, rather than as a result of, the Gap storm downburst. A comparison of the CP2 scans with the Mount Stapylton scans supports this interpretation as the strong near-surface winds are oriented *toward* the low.

The near-surface horizontal perturbation pressure gradient conceptually increases with 1) a more intense low-level circulation, 2) a more intense downdraft, 3) a colder downdraft, and 4) a smaller distance between the mesohigh and the mesolow. We will now show that the storm-relative wind field reported in association with many high-end straight-line wind events might play a role in the enhancement of the perturbation pressure gradient.

A peculiar characteristic of largely nontornadic destructive wind storms is a storm-relative flow in the inflow layer that substantially exceeds the midlevel storm-relative flow (Evans and Doswell 2001; Conway et al. 1996; Lemon and Parker 1996; Brooks and Doswell 1993; Coniglio et al. 2011).

Figure 18 shows that the storm-relative flow for the Gap storm exceeded $10\,\mathrm{m\,s^{-1}}$ through a depth of the lowest 200 hPa above the ground, transporting high (<20°C) surface dewpoints and high ($<12\,\mathrm{g\,kg^{-1}}$) mixing ratios through 70 hPa (Fig. 4) into the updrafts of the Gap storm prior to the wind event (Fig. 6b). Consistent with these observations, Coniglio et al. (2011) conclude that exceptionally high moisture fluxes into the 8 May 2009 derecho updrafts associated with a strong low-level jet were instrumental in the creation of the damaging surface winds through primarily a strengthening of the updrafts themselves.

The strong storm-relative winds for the Gap storm in the 0533 UTC sounding (Fig. 18) also increased the storm-relative helicity (SRH; Davies-Jones 1984) values with the 0–3-km SRH of $-134\,\mathrm{m^2\,s^{-2}}$. The supply of streamwise low-level vorticity suggests at least some potential for storm-scale rotation, as is evident in Fig. 16. The diminished values of SRH in the 0628 UTC AMDAR hodograph (Fig. 18) representative of the near-coastal wind profile (Fig. 14) might have contributed to the Gap storm's decline after 0648 UTC, alongside increasingly cooler low-level inflow and a strengthening cap as the storm approached the coastline given its motion vector toward 20°.

Similar to the aforementioned Lahoma or Pakwash storms, for example, the Gap storm also exhibited light midlevel storm-relative winds below $8\,\mathrm{m\,s^{-1}}$ in the 770–620-hPa layer (Fig. 18). Light storm-relative winds are commonly observed with storms that produce strong

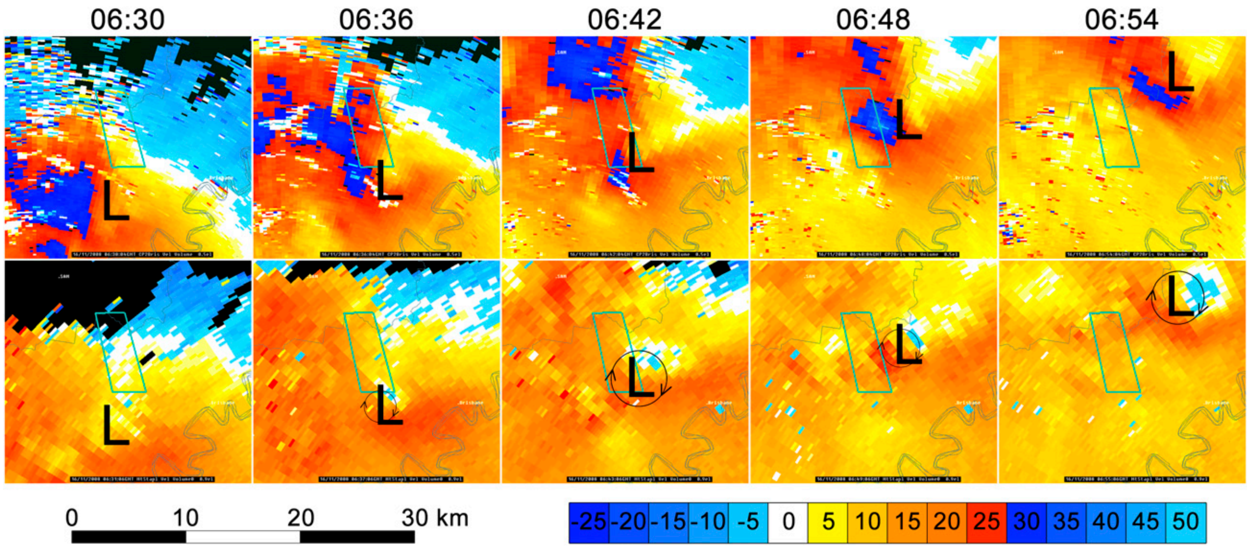

FIG. 17. (top) Ground-relative radial winds ($m s^{-1}$) seen by the CP2 radar (0.5° tilt) and (bottom) storm-relative radial winds ($m s^{-1}$) seen by the Mount Stapylton radar (0.9° tilt) at times (column 1) 0630, (column 2) 0636, (column 3) 0642, (column 4) 0648, and (column 5) 0654 UTC. The storm moves at $10 m s^{-1}$ from 200°. The circulations across the bottom row have been fit subjectively to match the velocity couplet. The storm-scale perturbation low (marked with an L) is placed at the center of the circulation and, at a given time, is in the same location for each column.

nontornadic winds, and they have been linked to the promotion of a strong cold pool in otherwise favorable thermodynamic environments (Evans and Doswell 2001), but also to the risk of an updraft being undercut by the surging cold pool (Brooks and Doswell 1993; Brooks et al. 1994, Thompson 1998). *The light storm-relative winds in the Gap storm case allowed the hail core and downdraft to descend to a location close to the low-level circulation, thus promoting a strong horizontal perturbation pressure gradient between the cold pool and the circulation near the ground.* A subsequent demise of the low-level circulation, which previously "channeled" the storm's outflow northward past its western flank while allowing continuing southbound inflow on its eastern flank (Fig. 17), would have allowed the outflow to surge northward and cut off the inflow into the Gap storm's updraft (see also the helicity discussion above).

6. Summary and conclusions

On 16 November 2008, an unusually intense windstorm with near-surface winds exceeding $43 m s^{-1}$ created widespread tree and roof damage about 10 km west-northwest of Brisbane, one of Australia's largest cities. The near-storm environment showed a number of similarities with previous nontornadic destructive windstorms associated with storm modes such as HP supercells (Conway et al. 1996; Lemon and Parker 1996) or derechos (Evans and Doswell 2001; Coniglio et al. 2011). It possessed relatively strong low-level storm-relative flow that transported very moist air with boundary layer mixing ratios exceeding $12 g kg^{-1}$ toward the storm's updraft, but only light ($<10 m s^{-1}$) midlevel storm-relative winds were present at the peak of the event. The wind-producing storm contained multiple updrafts, some of which exhibited severity-indicating radar signatures such as bounded weak echo regions (BWERs), three-body scatter spikes (TBSSs) or a reflectivity value exceeding 70 dBZ and reduced correlation coefficients ρ_{hv} within the hail growth layer between −10° and −30°C. Apart from transient circulations, midlevel mesocyclones were largely absent, while a more persistent low-level circulation pattern was present at the time of the destructive winds.

Separate wind-promoting mechanisms acted in aggregate to produce the observed destructive winds (Fig. 19). Very moist strong storm-relative low-level flow allowed the formation of strong updrafts and elevated cores containing large hail. Upon descent, the hail core encountered a thermodynamic environment largely favorable for the formation of a cold and intense downdraft. The core started to melt high above the ground due to the relatively high melting level (~4 km AGL). The ambient lapse rates below the melting level approached a dry adiabat through a depth of about 150 hPa, ensuring that the downdraft (fueled by melting hail and subsequent evaporation of liquid water) would remain negatively buoyant. Further cooling potential was present as the liquid water present experienced a layer of dry ambient air about 2–3 km below the melting level. Near the

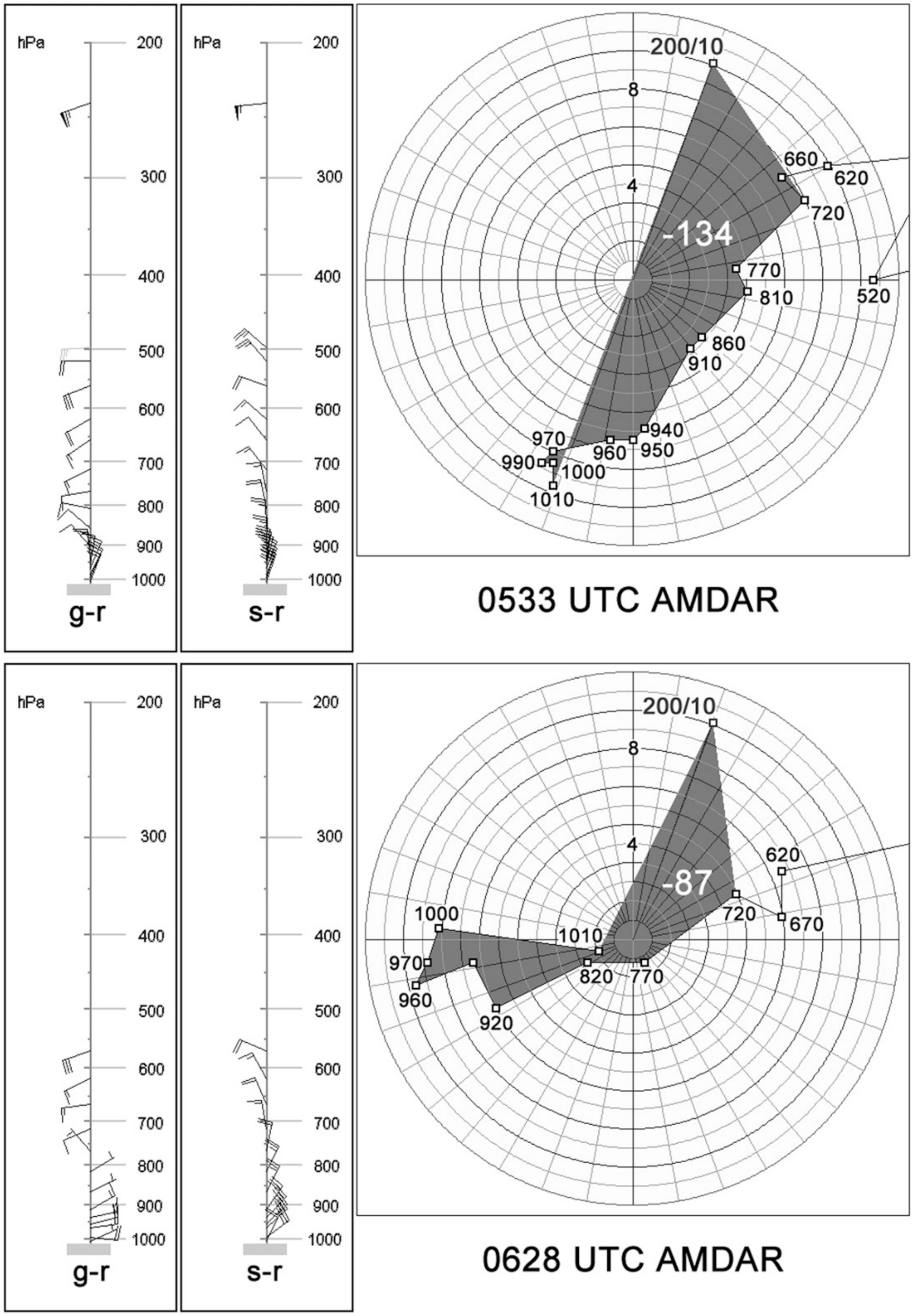

FIG. 18. Profiles of the ground-relative (''g-r'') and storm-relative (''s-r'') flows and corresponding hodographs constructed from the (top) 0533 and (bottom) 0628 UTC AMDAR aircraft data. The SRH for inflow extending from the surface up to 700 hPa (approximately 0–3 km) assuming a storm motion of 10 m s^{-1} from 200° is printed inside the shaded area, which, in itself, is proportional to the SRH. Pressure levels are annotated at each level (in hPa). Long wind barbs denote 5 m s^{-1}, and short wind barbs for 2.5 m s^{-1}.

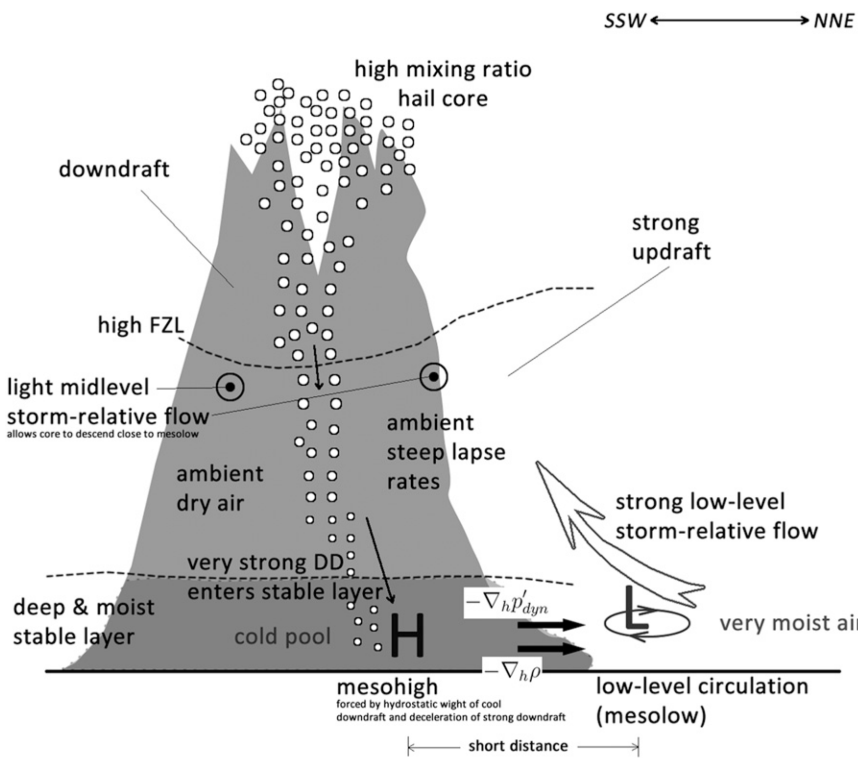

FIG. 19. Conceptual diagram of the various contributions to the destructive surface winds in the Gap storm. The light shading marks the overall downdraft location, and the dark shading the storm's cold pool. The downdraft is not hydrometeor supply limited and can take advantage of the cooling effect of melting and evaporating hail. The light storm-relative winds at midlevels (blowing out of the page) allow the mesohigh to set up in close proximity to the circulation-forced mesolow, which enhances the horizontal gradient of the dynamically forced component of the perturbation pressure. The horizontal density gradient shown is mainly forced by the deep and cool cold pool.

ground, however, the presumably strong downdraft interacted with a stably stratified layer that was almost 1 km deep, which would have led to downdraft weakening near the ground.

However, with the 65–70-dBZ hail core descending all the way to the surface, the downdraft forcing due to condensate loading is no longer negligible. This finding relates to a similar conclusion in Coniglio et al. (2011) that in environments with limited evaporation potential, hydrometeor loading and melting of abundant ice might play an important role in downdraft mass fluxes.

We suggest that the acceleration of the deep cold pool in the direction of the maximum horizontal density gradient (broadly northward) was augmented by the presence of a persistent low-level circulation pattern to the northeast of the cold-pool-related mesohigh. The close proximity of the hydrostatically and dynamically driven mesohigh at the base of the downdraft to the dynamically driven mesolow associated with the low-level circulation is hypothesized to have been instrumental in the observed anisotropic horizontal acceleration of the near-ground outflow and the ultimate strength of the Gap storm surface winds. The downdraft descent close to the updraft would have been promoted by the light midlevel storm-relative winds, which accounted for relatively small lateral hydrometeor displacements from their original horizontal positions in the upper regions of the updraft.

The physical concepts discussed through this study should now be further substantiated through a convection-permitting model that assimilates the Mount Stapylton and CP2 Doppler data. We hope to progress to such a study in the near future.

Acknowledgments. This study was supported by funding from the Weather and Environmental Prediction (WEP) program as part of the Centre for Australian Weather and Climate Research (CAWCR). In particular, the authors applaud Dr. Peter May for his continuous prodding and consequential advancement of the manuscript. The lead author would also like to thank various members of the VORTEX-2 team for discussions on wind storms with weak storm-relative midlevel winds. We also thank Matt Kumjian, Michael Coniglio, and an anonymous reviewer for substantially strengthening the initial manuscript.

Argonne National Laboratory's work was supported by the U.S. Department of Energy, Office of Science, Office of Biological and Environmental Research, under Contract DE-AC02-06CH11357. This work has been supported by the Office of Biological and Environmental Research (OBER) of the U.S. Department of Energy (DOE) as part of the ARM Program.

APPENDIX

Downdraft Acceleration due to Hail Loading

Based on the exponential hailstone size distribution specified in Lin et al. (1983) and later used (in integrated form) in Gao and Stensrud (2012), we express the hail-mixing ratio q_H (in $\mathrm{kg\,kg^{-1}}$) as a single-moment relation:

$$q_H = \frac{1}{\rho}\left(\frac{10^{Z_{\mathrm{dB}}/10}}{4.33\times 10^{10}}\right)^{4/7}, \tag{A1}$$

where ρ is the air density ($\mathrm{kg\,m^{-3}}$) and Z_{dB} the (logarithmic) reflectivity factor (in dBZ).

The hail-mixing ratio q_H forms one part of the buoyancy term in the Boussinesq form of the vertical momentum equation (Houze 1993):

$$\frac{Dw}{Dt} = -\frac{1}{\rho_0}\frac{\partial p'}{\partial z} + g\left(\frac{T'}{T_0} + \frac{p'}{p_0} + 0.608q_{\mathrm{vap}} - q_H\right) + F_z, \tag{A2}$$

where w is the vertical velocity of the downdraft parcel ($w > 0$ implies upward motion); (ρ_0; T_0, p_0) are the hydrostatically balanced components of the full downdraft parcel density ρ, temperature T, and pressure p; $p' = p - p_0$ is the deviation of the parcel's total pressure from the hydrostatically balanced value; q_{vap} is the water vapor mixing ratio; g the acceleration due to gravity; and F_z parameterizes the residual downdraft parcel forcing that has not been captured through the perturbation pressure or buoyancy forcing terms. Note that q_H in Eq. (A2) strictly denotes the total hydrometeor loading (hail, graupel, ice, liquid water), but based on the analysis in section 5b we treat the core as consisting entirely of large hail.

To crudely estimate the magnitude of the downdraft velocities w_H achievable due to the *hail-loading term only*, we integrate the simplified vertical momentum equation

$$\frac{Dw_H}{Dt} = -gq_H \tag{A3}$$

between the level of origin of the hail core z_i and the ground at $z = 0\,\mathrm{m}$. An analytical solution to Eq. (A3) can be achieved when the ambient vertical density profile,

$$\rho_0(z) = \frac{p_*}{R_d T_*}\left(1 - \frac{\gamma}{T_*}z\right)^{(g/\gamma R_d)-1}, \tag{A4}$$

based on the International Standard Atmosphere (ISA), is used. Here, $T_0(z) = T_* - \gamma z$ is the ambient vertical temperature profile, $T_* = 288.15\,\mathrm{K}$ is the surface temperature, $\gamma = 6.5 \times 10^{-3}\,\mathrm{K\,m^{-1}}$ is the constant lapse rate, z (m) is the height above ground level, $p_* = 101\,325\,\mathrm{Pa}$ is the surface pressure, $R_d = 287\,\mathrm{J\,kg^{-1}\,K^{-1}}$ is the specific gas constant for dry air, and $g = 9.81\,\mathrm{m\,s^{-2}}$ is the acceleration due to gravity.

Equations (A1) and (A4) allow us to rewrite Eq. (A3) in a form that relates the downdraft parcel acceleration explicitly to the hail-related reflectivity returns Z_{dB}:

$$\frac{d^2 z_H}{dt^2} = -\frac{g}{a(b - z_H)^c}\left(\frac{10^{Z_{\mathrm{dB}}/10}}{4.33\times 10^{10}}\right)^{4/7}, \tag{A5}$$

where z_H (m) is the height above ground level for a downdraft parcel forced only by the hail-loading term, $c = (g/\gamma R_d) - 1 = 4.256\,85$, $b = T_*/\gamma = 44\,330.8\,\mathrm{m}$, and $a = (p_*/R_d T_*)(\gamma/T_*)^c \sim 2.0319 \times 10^{-20}\,\mathrm{kg\,m^{-(3+c)}}$.

The substitutions $\phi = b - z_H$ and $\nu = d\phi/dt$ convert Eq. (A5) into a first-order ordinary differential equation that has the solution

$$w_{\max} = +\sqrt{\frac{2K(Z_{\mathrm{dB}})}{1-c}([b - z_i]^{1-c} - b^{1-c})}, \tag{A6}$$

where $w_{\max}$ is the magnitude of the maximum downdraft speed at the surface and $K(Z_{\mathrm{dB}}) = (g/a)(10^{Z_{\mathrm{dB}}/10}/4.33\times 10^{10})^{4/7}$.

REFERENCES

Benjamin, T. B., 1968: Gravity currents and related phenomena. *J. Fluid Mech.*, **31,** 209–248, doi:10.1017/S0022112068000133.

Blair, S. F., D. R. Deroche, J. M. Boustead, J. W. Leighton, B. L. Barjenbruch, and W. P. Gargan, 2011: A radar-based assessment of the detectability of giant hail. *Electron. J. Severe Storm Meteor.,* **6** (7). [Available online at http://www.ejssm.org/ojs/index.php/ejssm/article/viewArticle/87.]

Bringi, V. N., and A. Hendry, 1990: Technology of polarization diversity radars for meteorology. *Radar in Meteorology,* D. Atlas, Ed., Amer. Meteor. Soc., 153–190.

Brooks, H. E., and C. A. Doswell III, 1993: Extreme winds in high precipitation supercells. Preprints, *17th Conf. on Severe Local Storms,* St. Louis, MO, Amer. Meteor. Soc., 173–177.

——, ——, and R. B. Wilhelmson, 1994: The role of midtropospheric winds in the evolution and maintenance of low-level mesocyclones. *Mon. Wea. Rev.,* **122,** 126–136, doi:10.1175/1520-0493(1994)122<0126:TROMWI>2.0.CO;2.

Coniglio, M. C., S. F. Corfidi, and J. S. Kain, 2011: Environment and early evolution of the 8 May 2009 derecho-producing convective system. *Mon. Wea. Rev.,* **139,** 1083–1102, doi:10.1175/2010MWR3413.1.

Conway, J. W., H. E. Brooks, and K. D. Hondl, 1996: The 17 August 1994 Lahoma, OK supercell: Issues of tornadogenesis and bow echo formation. Preprints, *18th Conf. on Severe Local Storms,* San Francisco, CA, Amer. Meteor. Soc., 52–56.

Davies-Jones, R. P., 1984: Streamwise vorticity: The origin of updraft rotation in supercell storms. *J. Atmos. Sci.,* **41,** 2991–3006, doi:10.1175/1520-0469(1984)041<2991:SVTOOU>2.0.CO;2.

Evans, J. S., and C. A. Doswell III, 2001: Examination of derecho environments using proximity soundings. *Wea. Forecasting,* **16,** 329–342, doi:10.1175/1520-0434(2001)016<0329:EODEUP>2.0.CO;2.

Eyre, L. A., 1992: How severe can a "severe thunderstorm" be?: An investigation into two violent electrical storms in Australia. *Weather,* **47,** 374–383, doi:10.1002/j.1477-8696.1992.tb07100.x.

Gao, J., and D. J. Stensrud, 2012: Assimilation of reflectivity data in a convective-scale, cycled 3DVAR framework with hydrometeor classification. *J. Atmos. Sci.,* **69,** 1054–1065, doi:10.1175/JAS-D-11-0162.1.

Houze, R. A., Jr., 1993: *Cloud Dynamics.* Academic Press, 570 pp.

——, 2004: Mesoscale convective systems. *Rev. Geophys.,* **42,** RG4003, doi:10.1029/2004RG000150.

Hubbert, J. C., S. M. Ellis, W.-Y. Chang, S. Rutledge, and M. Dixon, 2014: Modeling and interpretation of S-band ice crystal depolarization signatures from data obtained by simultaneously transmitting horizontally and vertically polarized fields. *J. Appl. Meteor. Climatol.,* **53,** 1659–1677, doi:10.1175/JAMC-D-13-0158.1.

Hurlbut, M., and A. Cohen, 2014: Environments of northeast U.S. severe thunderstorm events from 1999 to 2009. *Wea. Forecasting,* **29,** 3–22, doi:10.1175/WAF-D-12-00042.1.

Johns, R. H., and W. D. Hirt, 1987: Derechos: Widespread convectively induced windstorms. *Wea. Forecasting,* **2,** 32–49, doi:10.1175/1520-0434(1987)002<0032:DWCIW>2.0.CO;2.

Kamburova, P. L., and F. H. Ludlam, 1966: Rainfall evaporation in thunderstorm downdrafts. *Quart. J. Roy. Meteor. Soc.,* **92,** 510–518, doi:10.1002/qj.49709239407.

Keeler, R. J., P. H. Herzegh, and C. L. Frush, 1984: Measurements of CP2 copolar and cross-polar antenna illumination functions at S and X band. Preprints, *22nd Conf. on Radar Meteorology,* Zurich, Switzerland, Amer. Meteor. Soc., 287–291.

——, B. W. Lewis, and G. R. Gray, 1989: Description of NCAR/FOF CP-2 meteorological Doppler radar. Preprints, *24th Conf. on Radar Meteorology,* Tallahassee, FL, Amer. Meteor. Soc., 589–592.

Keenan, T., J. W. Wilson, J. Lutz, K. Glasson, and P. T. May, 2007: Rationale and use of the CP2 testbed in Brisbane, Australia. *33rd Conf. on Radar Meteorology,* Cairns, QLD, Australia, Amer. Meteor. Soc., 12B.1. [Available online at http://ams.confex.com/ams/33Radar/techprogram/paper_123253.htm.]

Kelly, D. L., J. T. Schaefer, and C. A. Doswell III, 1985: Climatology of nontornadic severe thunderstorm events in the United States. *Mon. Wea. Rev.,* **113,** 1997–2014, doi:10.1175/1520-0493(1985)113<1997:CONSTE>2.0.CO;2.

Kingsmill, D., 1995: Convection initiation associated with a sea-breeze front, a gust front, and their collision. *Mon. Wea. Rev.,* **123,** 2913–2933, doi:10.1175/1520-0493(1995)123<2913:CIAWAS>2.0.CO;2.

Klemp, J. B., and R. Rotunno, 1983: A study of the tornadic region within a supercell thunderstorm. *J. Atmos. Sci.,* **40,** 359–377, doi:10.1175/1520-0469(1983)040<0359:ASOTTR>2.0.CO;2.

Leitch, C., G. Ginger, B. Harper, P. Kim, N. Jayasinghe, and L. Somerville, 2009: Investigation of performance of housing in Brisbane following storms on 16 and 19 November 2008. School of Engineering and Physical Sciences Technical Rep. 55, James Cook University, Townsville, QLD, Australia, 76 pp.

Lemon, L. R., 1998: The radar "three-body scatter spike": An operational large-hail signature. *Wea. Forecasting,* **13,** 327–340, doi:10.1175/1520-0434(1998)013<0327:TRTBSS>2.0.CO;2.

——, and S. Parker, 1996: The Lahoma storm deep convergence zone: Its characteristics and role in storm dynamics and severity. Preprints, *18th Conf. on Severe Local Storms,* San Francisco, CA, Amer. Meteor. Soc., 70–75.

Lin, Y.-L., R. D. Farley, and H. D. Orville, 1983: Bulk parameterization of the snow field in a cloud model. *J. Climate Appl. Meteor.,* **22,** 1065–1092, doi:10.1175/1520-0450(1983)022<1065:BPOTSF>2.0.CO;2.

Lindley, T. T., and L. R. Lemon, 2007: Preliminary observations of weak three-body scatter spikes associated with low-end severe hail. *Electron. J. Severe Storms Meteor.,* **2** (3). [Available online at http://www.ejssm.org/ojs/index.php/ejssm/article/viewArticle/12.]

Markowski, P. M., 2002: Hook echoes and rear-flank downdrafts: A review. *Mon. Wea. Rev.,* **130,** 852–876, doi:10.1175/1520-0493(2002)130<0852:HEARFD>2.0.CO;2.

Moller, A. R., C. A. Doswell III, and R. Przybylinski, 1990: High-precipitation supercells: A conceptual model and documentation. Preprints, *16th Conf. on Severe Local Storms,* Kananaskis Park, AB, Canada, Amer. Meteor. Soc., 52–57.

——, ——, M. P. Foster, and G. R. Woodall, 1994: The operational recognition of supercell thunderstorm environments and storm structures. *Wea. Forecasting,* **9,** 327–347, doi:10.1175/1520-0434(1994)009<0327:TOROST>2.0.CO;2.

Pepler, A. S., and P. T. May, 2012: A robust error-based rain estimation method for polarimetric radar. Part II: Case study. *J. Appl. Meteor. Climatol.,* **51,** 1702–1713, doi:10.1175/JAMC-D-11-0159.1.

Phillips, B. B., 1973: Precipitation characteristics of a sheared, moderate intensity, supercell-type Colorado thunderstorm. *J. Appl. Meteor.,* **12,** 1354–1363, doi:10.1175/1520-0450(1973)012<1354:PCOASM>2.0.CO;2.

Proctor, J. F. W., 1989: Numerical simulations of an isolated microburst. Part II: Sensitivity experiments. *J. Atmos. Sci.,* **46,** 2143–2165, doi:10.1175/1520-0469(1989)046<2143:NSOAIM>2.0.CO;2.

Rotunno, R., and J. B. Klemp, 1982: The influence of the shear-induced pressure gradient on thunderstorm motion. *Mon. Wea. Rev.,* **110,** 136–151, doi:10.1175/1520-0493(1982)110<0136:TIOTSI>2.0.CO;2.

——, and ——, 1985: On the rotation and propagation of simulated supercell thunderstorms. *J. Atmos. Sci.,* **42,** 271–292, doi:10.1175/1520-0469(1985)042<0271:OTRAPO>2.0.CO;2.

Ryzhkov, A. V., and D. S. Zrnić, 2007: Depolarization in ice crystals and its effect on radar polarimetric measurements.

J. Atmos. Oceanic Technol., **24,** 1256–1267, doi:10.1175/JTECH2034.1.

——, M. R. Kumjian, S. M. Ganson, and A. P. Khain, 2013: Polarimetric radar characteristics of melting hail. Part I: Theoretical simulations using spectral microphysical modeling. *J. Appl. Meteor. Climatol.,* **52,** 2849–2870, doi:10.1175/JAMC-D-13-073.1.

Srivastava, R. C., 1985: A simple model of evaporatively driven downdraft: Application to microburst downdraft. *J. Atmos. Sci.,* **42,** 1004–1023, doi:10.1175/1520-0469(1985)042<1004:ASMOED>2.0.CO;2.

——, 1987: A model of intense downdrafts driven by the melting and evaporation of precipitation. *J. Atmos. Sci.,* **44,** 1752–1774, doi:10.1175/1520-0469(1987)044<1752:AMOIDD>2.0.CO;2.

Tessendorf, S. A., and Coauthors, 2012: The Queensland Cloud Seeding Research Program. *Bull. Amer. Meteor. Soc.,* **93,** 75–90, doi:10.1175/BAMS-D-11-00060.1.

Thompson, R. L., 1998: Eta Model storm-relative winds associated with tornadic and nontornadic supercells. *Wea. Forecasting,* **13,** 125–137, doi:10.1175/1520-0434(1998)013<0125:EMSRWA>2.0.CO;2.

——, R. Edwards, J. A. Hart, K. L. Elmore, and P. M. Markowski, 2003: Close proximity soundings within supercell environments obtained from the Rapid Update Cycle. *Wea. Forecasting,* **18,** 1243–1261, doi:10.1175/1520-0434(2003)018<1243:CPSWSE>2.0.CO;2.

Tuttle, J. D., and C. A. Davis, 2006: Corridors of warm season precipitation in the central United States. *Mon. Wea. Rev.,* **134,** 2297–2317, doi:10.1175/MWR3188.1.

Wakimoto, R. M., 2001: Convectively driven high winds. *Severe Convective Storms, Meteor. Monogr.,* No. 50, Amer. Meteor. Soc., 255–298.

——, and V. N. Bringi, 1988: Dual-polarization observations of microbursts associated with intense convection: The 20 July storm during the MIST project. *Mon. Wea. Rev.,* **116,** 1521–1539, doi:10.1175/1520-0493(1988)116<1521:DPOOMA>2.0.CO;2.

——, W.-C. Lee, H. B. Bluestein, C.-H. Liu, and P. H. Hildebrand, 1996: ELDORA observations during VORTEX 95. *Bull. Amer. Meteor. Soc.,* **77,** 1465–1481, doi:10.1175/1520-0477(1996)077<1465:EODV>2.0.CO;2.

Zrnić, D. S., V. N. Bringi, N. Balakrishnan, K. Aydin, V. Chandrasekar, and J. Hubbert, 1993: Polarimetric measurements in a severe hailstorm. *Mon. Wea. Rev.,* **121,** 2223–2238, doi:10.1175/1520-0493(1993)121<2223:PMIASH>2.0.CO;2.